AIAA JOURNAL
Vol. 41, No. 3, March 2003

Comparison of Heat Transfer Augmentation Techniques

P. M. Ligrani and M. M. Oliveira
University of Utah, Salt Lake City, Utah 84112-9208
and
T. Blaskovich
Pratt and Whitney Canada, United Technologies Corporation, Longueuil, Quebec J4G 1A1, Canada

Nomenclature

a	=	streamwise extent of test surface
b	=	spanwise extent of test surface
D	=	dimple print diameter
D_h	=	channel hydraulic diameter
d	=	pin fin diameter
e	=	rib turbulator width and height
e'	=	rib turbulator width in streamwise direction
f	=	friction factor
f	=	vortex pair shedding frequency
f_0	=	baseline friction factor in a smooth channel with no augmentation devices
H	=	channel height
h	=	rib height
L	=	upstream (smallest axial) location of axial/radial measurement or visualization plane in the swirl chamber, measured from $x = 0$
Nu	=	local Nusselt number based on channel hydraulic diameter
Nu_0	=	baseline, constant property Nusselt number in a smooth channel with no augmentation devices
P	=	static pressure
p	=	streamwise pitch spacing of rib turbulators, or streamwise spacing of pin fin centers

Dr. Phil Ligrani is currently Professor of Mechanical Engineering and Director of the Convective Heat Transfer Laboratory at the University of Utah and a Fellow of the American Society of Mechanical Engineers. He has been working on convection heat transfer and fluid mechanics research problems since he received his Ph.D. degree from the Department of Mechanical Engineering at Stanford University in 1980. From 1979 to 1982, he was an Assistant Professor in the Turbomachinery Department of the von Kármán Institute for Fluid Dynamics, Rhode-Saint-Genese, Belgium. From 1982 to 1984, he worked in the Department of Aeronautics of the Imperial College of Science and Technology, University of London. From 1984 to 1992, he was an Associate Professor in the Department of Mechanical Engineering of the U.S. Naval Postgraduate School. In his research, he has investigated the ultra-small-scale motions that exist near walls in turbulent boundary layers, the effects of surface roughness on turbulent boundary layers, transitional phenomena in curved channels including the development and structure of Dean vortex pairs, and innovative schemes for internal cooling and surface heat transfer augmentation, such as dimpled surfaces and swirl chambers, as well as a variety of gas turbine heat transfer and blade cooling problems. He served as Guest Editor for the journal *Measurement Science and Technology* from 1998 to 2000, and he will serve as Associate Technical Editor for the *Journal of Heat Transfer* from 2003 to 2006. He has published approximately 150 journal papers, conference papers, and book chapters. In 1995, he was presented with the "Professor of the Year" award at the University of Utah for outstanding classroom teaching. Some of his other activities and recognitions include a Guest Professorship in 2000 at the Institut für Thermische Stroemungsmaschinen-Universitaet Karlsruhe, a Visiting Senior Research Fellowship from 1982 to 1983 at the Imperial College of Science and Technology–University of London, a NASA Space Act Tech Brief Award in 1991 for "Development of Subminiature Multi-Sensor Hot-Wire Probes," and the Carl E. and Jessie W. Menneken Faculty Award in 1990 for Excellence in Scientific Research. E-mail: ligrani@mech.utah.edu.

Mauro Oliveira received his B.S. degree in mechanical engineering from the University of Utah in 1998 and his M.S. degree in mechanical engineering from the University of Utah in 2002. His research efforts at the University of Utah focused on augmentation of heat transfer in internal passages, mainly using arrays of hemispherical dimples.

Tim Blaskovich has worked in the gas turbine industry since graduating with a B. Eng. honors degree from McGill University in 1995. His experience at Pratt and Whitney Canada has included mechanical design of turbines, transmissions, and externals/accessories and, to a larger extent, aerothermal design and analysis of turbine airfoils. His research in the field of turbine cooling and durability has included characterization of advanced coatings, development of a transient heat transfer facility utilizing thermochromic liquid crystals, and development of advanced computational fluid dynamics methods for cooled turbines. From 1999 to 2001, he had the privilege of being the overall turbine technology manager, responsible for short- to long-term planning of research programs and phasing of new technology into the next generation of small gas turbine engines. Most recently, he received his M. Eng. degree in Mechanical Engineering from McGill University, where his project involved theoretical and numerical work on the topic of magnetohydrodynamics applied to the case of electromagnetic separation of inclusions from molten metal.

Received 19 September 2002; revision received 15 October 2002; accepted for publication 23 October 2002.

p' = streamwise spacing between adjacent pin fins
Re = Reynolds number based on swirl chamber inlet duct hydraulic diameter, inlet duct time-averaged flow velocity, and inlet duct flow characteristics
Re_{Dh} = Reynolds number based on hydraulic diameter and mean velocity at test section inlet
Re_d = Reynolds number based on pin fin diameter and mean velocity at minimum flow area
Re_H = Reynolds number based on channel height and mean velocity at test section inlet
r = radial distance measured from swirl chamber centerline
r_0 = radius of the large cylinder comprising the swirl chamber
s = spanwise spacing of pin fin centers
s' = spanwise spacing between adjacent pin fins
T = local static temperature
U_b = streamwise bulk velocity averaged over the channel cross section
$\bar{U}$ = spatially averaged streamwise velocity
u = streamwise velocity
$\bar{u}$ = local time-averaged streamwise velocity
u' = local streamwise velocity fluctuation
$\bar{v}$ = local time-averaged normal velocity
v' = local normal velocity fluctuation
$\bar{w}$ = local time-averaged spanwise velocity
x, X = streamwise coordinate measured from the test section inlet, or axial distance measured from swirl chamber end face
y, Y = normal coordinate measured from the test surface
z, Z = spanwise coordinate measured from the test surface centerline
δ = dimple depth
ρ = density
ψ = circumferential angle measured from swirl chamber vertical plane
ω_x = streamwise vorticity

Subscripts

a = ambient value, or value at test facility inlet
w = local wall value
0 = baseline value, or stagnation value
$0i$ = total or stagnation value at the test section inlet

Superscripts

$\overline{}$ = time-averaged value
$\overline{\overline{}}$ = globally averaged value

Introduction

A VARIETY of techniques are used for enhancing convective heat transfer rates in gas turbine engine passages used for internal cooling of turbine airfoils. These include rib turbulators, pin fins, dimpled surfaces, surfaces with arrays of protrusions, swirl chambers, and surface roughness. All of these devices act to increase secondary flows and turbulence levels to enhance mixing, in some cases, to form coherent fluid motions in the form of streamwise oriented vortices. Such vortices and secondary flows not only act to increase secondary advection of heat away from surfaces, but also to increase three-dimensional turbulence production by increasing shear and creating gradients of velocity over significant flow volumes. These then give larger magnitudes of turbulence transport over larger portions of the flowfields. All of the devices mentioned also provide some heat transfer augmentation by increasing surface areas for convective heat transfer. The overall objective of each device is then significant enhancement of turbulence transport and convective heat transfer coefficients, with minimal increases in streamwise pressure drop penalties and skin-friction coefficients. Such heat transfer enhancements are needed for efficient heat load management, so that internal cooling air can remove the heat loads from turbine airfoil components. The best schemes give high cooling effectiveness with minimal coolant mass flow rates.

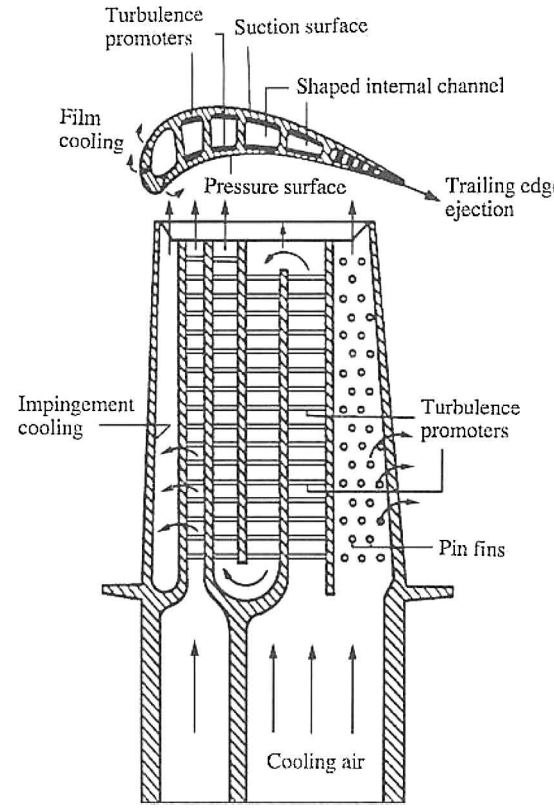

Fig. 1 Typical internal cooling arrangement for a multipass turbine blade; from Han et al.[1,2]

Figure 1 shows a typical internal cooling arrangement for a multipass turbine blade from Han et al.[1,2] The cooling air enters the airfoil through the blade root and then passes through one of several internal passages. In the high-pressure portion of the turbine, this cooling air generally originates at the compressor exit. Because of the blade shape, the cooling passages at many locations are generally confined and are, therefore, difficult to cool. These cooling passages also generally have complex cross-sectional shapes because they must be compatible with the external contours of the turbine airfoils. Features that provide the highest heat transfer coefficients for a given flow rate are required in the leading- and trailing-edge cavities of airfoils that may or may not be film cooled. The leading-edge geometry is characterized by a small coolant metal area to hot gas metal area ratio, whereas a thin trailing edge creates geometric constraints on passage sizes and accessibility for cooling air. For this reason, impingement cooling and swirl chambers are typically employed near the leading edge of the airfoil, either together or individually, and pin fins and exotic rib turbulator shapes are typically found near the trailing-edge regions of the airfoil. Rib tubulators, or turbulence promoters, are also located in passages near the midchord parts of the airfoil. Dimples and/or shaped roughness elements are also sometimes employed in all interior parts of airfoils, either by themselves or in conjunction with other devices. After passing over or through these devices, the cooling air then either exits through film cooling holes, or though exit passages that lead to another part of the airfoil.

In many cases, turbine airfoil cooling requires an effective combination of film cooling and internal cooling features that varies as the gas temperature is reduced through the turbine stages. Internal cooling is used by itself only when the mainstream temperature is low enough so that the heat load can be reduced and the leading and trailing edges can be cooled completely using internal convection alone. Inlet pressures in airfoil cooling passages are generally limited by the proximity of the coolant source and complexity of the ducting required to supply the coolant (along with associated weight and cost penalty). On the other hand, the use of coolant from a lower pressure source sometimes improves the thermal efficiency of the engine because less expensive air is used for cooling and more expensive air can then be used to do useful work through the turbine.

The present paper provides comparisons of heat transfer augmentations, friction factor augmentations, and thermal performance parameters provided by different devices used for internal cooling of turbine airfoils, including rib turbulators, pin fins, dimpled surfaces, surfaces with arrays of protrusions, swirl chambers, and surface roughness. To characterize the heat transfer augmentations, the ratio of the Nusselt number of the channel with augmenters divided by the Nusselt number of a similar smooth channel (at the same experimental conditions), Nu/Nu_0, is employed. Likewise, the increase in pressure losses is represented by the ratio of the friction factor measured in a channel with the augmenters divided by the friction factor of a similar smooth channel at the same experimental conditions, f/f_0. Such Nusselt number and friction factor ratios provide means to compare different techniques, as well as the performance of a given technique at different experimental conditions.

The present review paper also describes the flow characteristics and mechanisms responsible for the heat transfer augmentations provided by different devices used for internal cooling of turbine airfoils. Also included are discussions of the results presented in recent publications in this area. This approach is taken because very little information is available on flow characteristics and mechanisms, even though the literature contains abundant information on the heat transfer behavior of such internal cooling devices. For additional information on the heat transfer characteristics of internal cooling schemes, the reader is referred to another recent review paper by Lau.[3]

The fluid mechanics mechanisms responsible for the heat transfer augmentations are needed so that turbulence models can be developed that accurately represent the flow and to provide physical understanding so that additional improvements to internal cooling schemes are possible. Details of the flowfield structure, thus, aid the development of numerical models and prediction schemes and provide important insight into the flow structural characteristics responsible for local heat transfer coefficient augmentations. Internal cooling schemes for turbine airfoils are also chosen for discussion because this is a rapidly evolving area of research, with many new developments from many institutions located throughout the world. In spite of the amount of information in these areas, there is still much room for improvement. Better and improved cooling configurations will lead to overall improvements in overall gas turbine engine efficiency, reliability, and durability. In addition, the area is important because schemes for internal cooling of turbine airfoils can also be used in other devices, such as combustion chambers, air conditioners, radiators, microscale heat exchangers, macroscale heat exchangers, devices for electronics cooling, and biomedical devices, to name only a few.

Pin-Fin Arrays

When employed for internal cooling, pin fins or pedestals are generally arranged into arrays and extend between two opposite walls of an internal cooling passage. Figures 2 and 3 show typical arrangements (all dimensions in millimeters), from Brigham and Van Fossen[4] and Ligrani and Mahmood,[5] respectively. Pin fins are generally used in the parts of turbine airfoils where higher levels of heat transfer augmentation are required and where high-pressure drops are tolerated and in many cases even desired. Trailing edges of airfoils fall into this category. High coolant Reynolds numbers, associated with high coolant pressure, are desirable for heat transfer.

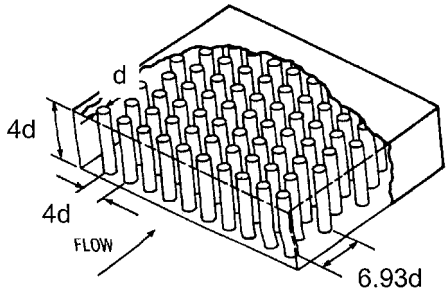

Fig. 2 Schematic diagram of typical pin-fin array employed in a channel, where $d = 0.318$ cm; from Brigham and Van Fossen.[4]

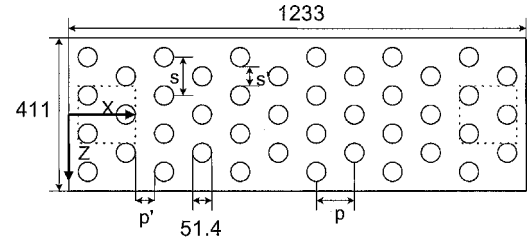

Fig. 3 Schematic diagram of the pin-fin test section from Ligrani and Mahmood,[5] including coordinate system and dimensions, which are given in millimeters: $s = 102.7$, $s' = 51.4$, $p = 102.7$, $p' = 51.4$, and flow direction left to right.

However, by the time the coolant reaches the trailing edge, it has often acquired a significant amount of heat, and the process of extracting heat from the cooling air is more challenging compared to other parts of the airfoil. At the same time, manufacturing limitations on the width of trailing-edge slots prevent adequate restriction for the coolant, thus requiring that the flow be metered upstream. Pin fins or pedestals are effective for allowing the pressure throughout most of the cooling circuit to remain high, while providing the necessary restriction near the trailing edge, to limit the coolant consumption to the desired level.

The large majority of existing pin fin investigations only focus on heat or mass transfer. Considered are the influences of pin geometry, pin materials, pin fin array configuration, channel geometry, different Reynolds numbers, and other parameters. Only a few recent studies examine fluid flow characteristics through passages with pin fins. Of the earlier heat transfer investigations, Zukauskas,[6] Sparrow et al.,[7] Metzger and Haley,[8] and Metzger et al.[9] report Nusselt numbers on flat surfaces as well as on pin surfaces and indicate the presence of large overall heat transfer augmentations for certain flow conditions and pin-fin array arrangements. Van Fossen[10] presents heat transfer coefficients measured on circular pin fins made of different materials, which are placed in rectangular cross-sectional channels. Different endwall plate-to-air temperature differences are employed. The Reynolds number dependence of the results is described, along with comparisons with available correlations for constant property conditions. Brigham and Van Fossen[4] report large overall heat transfer and mass transfer augmentations for circular pin fins arranged in in-line and staggered arrays. In another study, Simoneau and Van Fossen[11] measure pin surface heat transfer coefficients and streamwise turbulence intensities as the test section gas temperature varies between 260 and 290 K. The authors describe the effects of changing the number of pin rows.

Later investigations by Lau et al.[12] and McMillin and Lau[13] consider the effects of bleed ejection on heat and mass transfer distributions and on streamwise pressure variations in a channel with circular pin fins. Chyu,[14] Chyu and Goldstein,[15] and Chyu et al.[16] measure surface mass transfer coefficients using naphthalene-sublimation measurement techniques. Local and spatially averaged mass transfer coefficients are reported for different pin-fin arrays, which provide evidence of large overall mass transfer augmentations for certain in-line and staggered circular arrays. Grannis and Sparrow[17] numerically simulate the two-dimensional flow and pressure fields around diamond-shaped pin fins. Olson[18] describes the behavior of helium flowing through a channel with pins at different wall-to-fluid temperature differences. Normalized pressure drop and wall Nusselt number data are presented as dependent on Reynolds number and wall heat flux magnitude. The investigators employ a temperature ratio/power law scheme to account for variations of thermophysical properties on measured Nusselt numbers. Chyu,[14] Grannis and Sparrow,[17] Chyu and Natarajan,[19] Chyu et al.,[20] Hwang and Lu,[21] Uzol and Camci,[22,23] Ligrani and Mahmood,[5] and Mahmood et al.[24] consider the effects of different pin-fin shapes on heat transfer and flow in internal passages. A variety of pin-fin shapes are considered, including circular,[5,14,19–24] pins with endwall fillets,[14] diamond,[17,19–21] three-dimensional protruding elements,[19] cubic,[19,20] and elliptical.[22,23] Of these studies, the one described by Hwang and Lu[21] is especially unique because three pin-fin configurations, each arranged in a staggered array, are

considered in a trapezoidal duct, both with and without lateral flow ejection. A more recent investigation by Ligrani and Mahmood[5] considers the effects of variable properties on endwall heat transfer in a channel with a pin-fin array. Such variable property effects are present when absolute viscosity, molecular thermal conductivity, specific heat, or static density change with channel location because of variations of the local static temperature. The study shows that local and spatially averaged Nusselt numbers increase significantly as ratio of inlet stagnation temperature to local surface temperature T_{0i}/T_w decreases.

Pin-Fin Array Flow Structure

Even though these studies provide much information on surface heat transfer and surface mass transfer distributions, very little information is available on flow structure and flow behavior in passages with arrays of pin fins. The few available, existing studies describe a complex array of flow features, all of which have different influences on turbulent transport and on local and spatially averaged surface heat transfer distributions.

Chyu and Natarajan[19] present mass transfer distributions and surface flow streakline patterns (obtained using an oil–graphite technique) around several different shapes of single protruding elements placed on an endwall, including a cylinder, a cube, a diamond, a pyramid, and a hemisphere. Surface visualizations around the cylinder are shown in Fig. 4 for a freestream velocity of about 20 m/s and a Reynolds number based on obstacle height of 1.7×10^4. Here, flow is approaching the cylinder from the upper right-hand corner of the photograph. The cylinder mimics the behavior of a single pin fin, with height equal to cylinder diameter. Traces of the primary and secondary horseshoe vortices wrapping around the base of the cylinder are evident. The primary vortex initiates at the upstream most boundary of the domain influenced by the cylinder. A dark line just ahead of the cylinder marks the boundary-layer separation line signifying the formation of the secondary vortex. Note that this is located as much as one cylinder diameter upstream of the cylinder. The low pressure in the near-wake region behind the cylinder entrains both horseshoe vortices toward the centerline, $Z/D_h = 0$. According to the authors,[19] also seen in this region are the two lobular structures, observed as two spots of dark (graphite) flow accumulation. These lobes are characterized by vigorous motion and rotate in opposite directions with respect to one another. According to these investigators, such flow structures are sometimes called arch-shaped or inverted "U" vortices.

Farther downstream, turbulent mixing in the wake is stronger along the spanwise direction than in the streamwise direction. Overall, Fig. 4 shows that a necklace-shaped flow pattern is present downstream of the cylinder. The shear layers that develop along the endwall near this location produce regions of high mixing and high turbulent transport. As shear layers advect downstream of the recirculation zone, part of the flow is diverted backward toward the cylinder while the remaining fluid proceeds downstream. According to these investigators,[19] the levels of such disturbances become

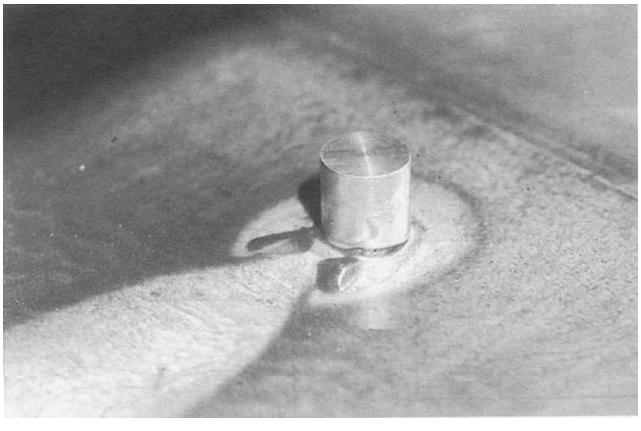

Fig. 4 Oil–graphite endwall visualizations from Chyu and Natarajan[19] for a cylinder placed on an endwall for a Reynolds number based on obstacle height of 1.7×10^4.

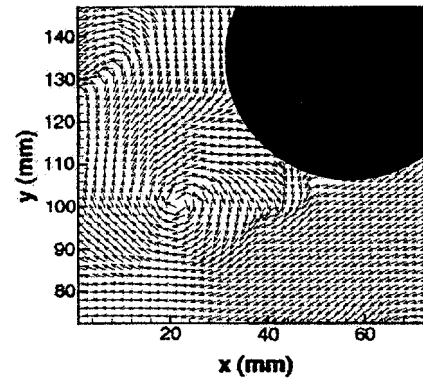

a) Instantaneous velocity vectors

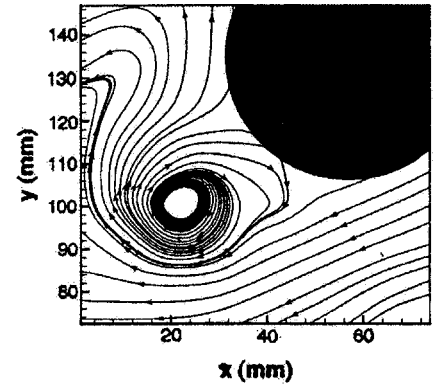

b) Instantaneous streamlines

Fig. 5 Measurement using particle image velocimetry by Uzol and Camci,[23] downstream of a one circular pin fin making up part of an array of pin fins arranged in two staggered rows for a Reynolds number based on cylinder diameter of 1×10^4.

lower as the boundary layer, which approaches the cylinder, becomes thicker.

The vortices and mixing present just downstream of pin fins are further elucidated by results presented by Uzol and Camci.[23] These investigators give flow structural characteristics measured using particle image velocimetry downstream of individual pin fins making up part of an array of pins arranged in two staggered rows. Cylindrical pin fins and pin fins with two different types of elliptical shapes are considered. Examples of results are shown in Fig. 5, which gives instantaneous velocity vectors and instantaneous streamlines downstream of a circular pin fin for a Reynolds number based on cylinder diameter of 1×10^4. The flow direction in Figs. 5a and 5b is from right to left in the direction of decreasing x coordinate. According to these authors,[23] early separation from the cylinder is apparent in these data plots. A shear layer is then apparent as the flow advects downstream. The velocity vectors within this shear layer, evident in Fig. 5b, show a distinct and irregular boundary between the high-speed flow outside of the wake and the low-speed flow within the wake. Embedded vortical structures are present within the shear layer near the edge of the wake, which are clearly evident in the secondary flow vectors in Fig. 5a and the streamlines in Fig. 5b. Notice that the axis of the largest vortex is parallel to the axis of the cylinder, which indicates that these structures are part of the arch-shaped or inverted U vortices, mentioned earlier. Because of this orientation and the direction of rotation of the vortices, the velocity vectors around the pin fin in Fig. 5b are directed away from the body of the pin fin. The resulting streamline arrangement then also has a pronounced effect on the separation location.

Figure 6 shows an instantaneous flow visualization image measured over a spanwise-normal plane (or flow cross-sectional plane) that is illuminated about four pin-fin diameters downstream of the last row of pin fins shown in Fig. 3 from Mahmood et al.[24] The image in Fig. 6 extends in the vertical direction from the bottom to the top of the channel and in the horizontal direction over a distance of about three channel heights. The spanwise center of the image

Fig. 6 Instantaneous flow visualization image illuminated over a spanwise-normal light plane located about four pin fin diameters downstream of the pin fin array shown in Fig. 2 for $Re_H = 430$; from Mahmood et al.[24]

is located at the spanwise center of the test section at $Z/D_h = 0$. Bulk flow motion in the streamwise direction is out of the plane of this image. This result is obtained for $Re_H = 430$ because diffusion and increased unsteadiness at higher Reynolds numbers result in smeared and unrecognizable flow patterns.

The most important features in Fig. 6 are two large vortex pairs (indicated by mushroom-shaped smoke patterns). One of these is on the right side of each image, and one is on the left side. The one on the right has an upwash region directed downward from the top wall, and the one on the left has an upwash region directed upward with respect to the bottom wall. These vortex pairs are formed by the effects of the pin fins, and the secondary flows within and around these vortices are especially intense because of the blockage effects produced by the pin fins. Note that a pin fin is located just upstream of the central part of the image shown in Fig. 6. The primary vortex pairs in Fig. 6 are the remnants (or downstream manifestations) of the two legs of the horseshoe vortices, described earlier. These legs are rearranged and reorganized by the arch-shaped or inverted U vortices that form just downstream of each pin fin. Patterns such as the one shown in Fig. 6 are, thus, produced by complex, unsteady secondary flows, which also rearrange distributions of streamwise velocity over a range of different length scales. As a result, shear gradients and mixing are spread over the entire channel cross section. With this in mind, the vortices and other secondary flows in the channel aid convective processes for heat transfer augmentation by 1) increasing secondary advection of fluid between the central parts of the channel and regions near the wall and 2) producing regions with high, three-dimensional shear and high magnitudes of turbulence production over much of the channel cross section, thereby substantially increasing turbulence transport levels in all three coordinate directions.

The secondary flows shown in Fig. 6 are consistent with the distribution of time-averaged streamwise vorticity presented in Fig. 7d, which is from Ref. 24. Also presented in Figs. 7a–7c are time-averaged surveys of streamwise velocity, total pressure, and static pressure. These are measured in a spanwise-normal plane located 0.5 pin-fin diameters downstream of the pin-fin array shown in Fig. 3 at a Reynolds number $Re_H = 8 \times 10^3$. Each of these surveys extends about one channel height in the vertical direction and about 3.5 channel heights in the horizontal direction. The primary vortex pairs, shown in Fig. 6, are responsible for the vorticity variations in Fig. 7d, where regions of positive and negative vorticity are positioned both near the top wall and near the bottom wall of the channel. Smaller vorticity signatures from other secondary vortices and vortex pairs are also apparent in Fig. 7. Each primary vortex pair is located near the edges of time-averaged shear layers evident in the surveys of local streamwise velocity and local total pressure in Figs. 7a and 7b, respectively. These time-averaged shear layers form at the edge of the wakes that develop behind the farthest downstream row of pin fins. The static pressure survey in Fig. 7c shows different variations, which are mostly a result of the curvature of the streamlines that develop downstream of the pin-fin array.

A schematic diagram of the flow features, deduced from these studies,[19,23,24] is presented in Fig. 8, for the pin-fin arrangement shown in Fig. 3. For this test section,[5] the channel aspect ratio is 8, and the short cylindrical pin fins extended from the channel bottom wall to the top wall. A total of 42 pins, each with uniform diameter and diameter to height ratio of 1 are used. The pins are placed in 12 rows in the streamwise direction, with 3 to 4 pins in each row.

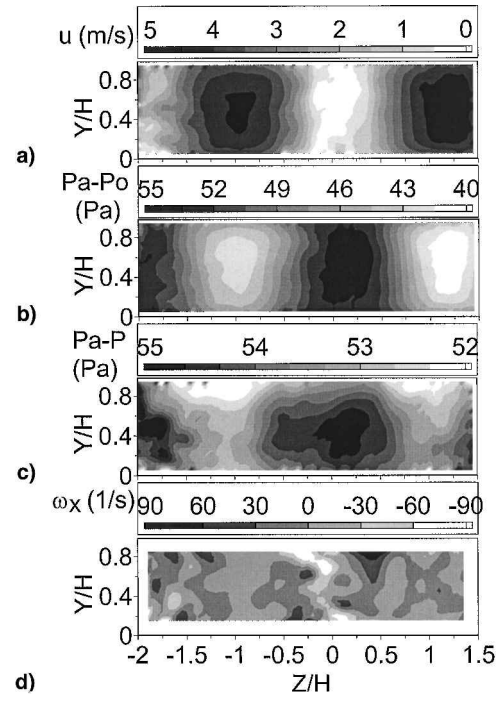

Fig. 7 Time-averaged surveys measured in a spanwise-normal plane located 0.5 pin-fin diameters downstream of the pin-fin array shown in Fig. 2 for $Re_H = 8000$; from Mahmood et al.[24]: a) streamwise velocity, b) total pressure, c) static pressure, and d) streamwise vorticity.

The spacing between adjacent pins, in both directions, equals the channel height. The centerline pin spacing (in both the streamwise and spanwise directions) is equal to twice the pin diameter and to 1.12 times the channel hydraulic diameter. The pin-fin test section is preceded by an inlet duct, with the same cross-sectional dimensions and a length of 13.3 hydraulic diameters.

Figure 8 shows the different flow structures that develop near one endwall junction of one pin fin. Similar phenomena are present near both endwall junctions of each and every pin fin. In the wake, which forms behind each pin fin, mixing is enhanced, and local velocities are relatively low, especially just downstream of each pin fin because of a flow recirculation zone. Farther downstream, local flow velocities increase, and large-scale unsteadiness forms with length scales approximately equal to the pin-fin diameter. At the edges of the wakes, shear layers are present where the low speed wake flow interfaces with higher speed flow away from the pin fins. These emanate in the streamwise flow direction from the spanwise edges of each pin. Here, turbulence production and transport are enhanced because of locally high levels of turbulent shear stress. Other key features of the flow are the primary and secondary horseshoe vortices that form upstream of each pin fin at the junction between the pin and the endwall. Here, strong secondary flows and secondary advection are provided by these vortices, as they advect away from the stagnation line located on the upstream pin-fin edge. Each leg of the primary horseshow vortex then advects within the shear layer that forms on either side of, and then, downstream of each pin fin. Arch shaped vortices are also shown in Fig. 8. The stagnation line on the upstream edge of each pin fin extends along the length of each pin fin. This is the initiation location for the thin boundary layers that begin to develop just downstream and then continue around each pin-fin cylinder. Eventually, the streamlines in each of these boundary layers separate from the cylinder at the locations where the downstream wake begins to form. The wakes, shear layers, and vortices, which form near the pin fins, increase mixing and turbulent transport as they are advected in the vicinity of pin fins located farther downstream.

Example of Spatially Resolved Surface Nusselt Number Distribution

A typical surface Nusselt number ratio distribution, produced on the endwall by the flow structures just described, is shown in Fig. 9. Here, spatially resolved Nusselt number ratios Nu/Nu_0 are given,

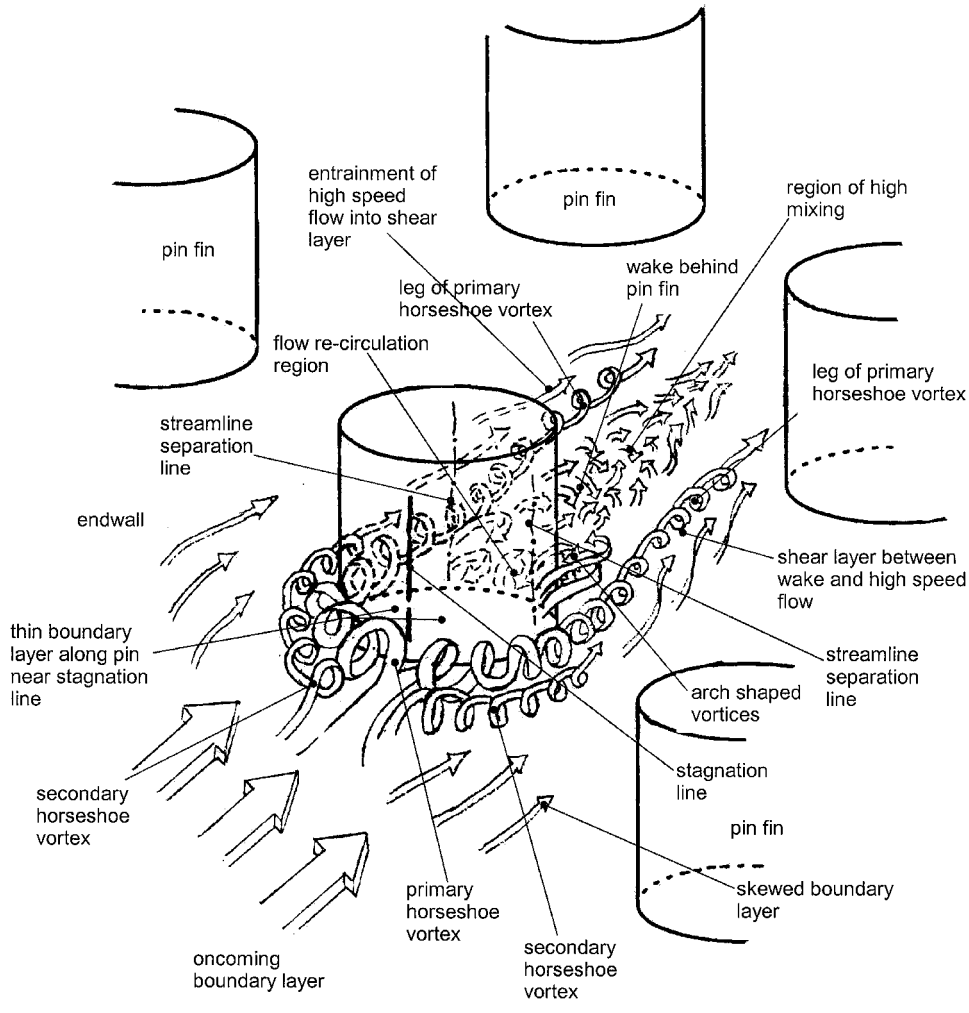

Fig. 8 Schematic diagram of flow features typically found in a channel with a staggered array of circular-cross-section pin fins.

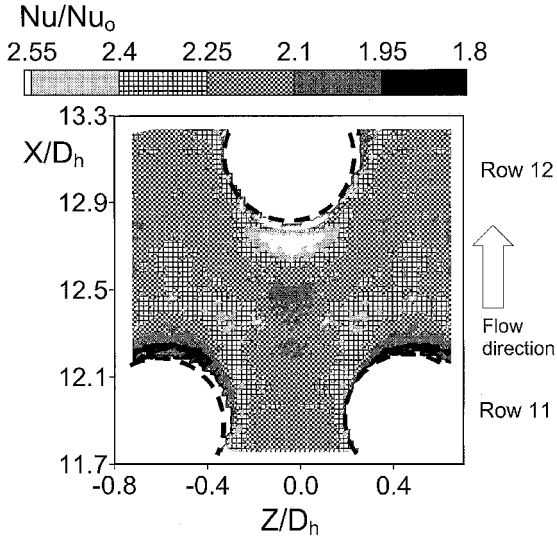

Fig. 9 Time-averaged local Nusselt number ratio Nu/Nu_0 distribution along the bottom pin-fin test surface for the arrangement shown in Fig. 2, from Ligrani and Mahmood,[5] for $Re_H = 1.83 \times 10^4$ and $T_{0i}/T_w = 0.93$.

which are measured by Ligrani and Mahmood[5] on one endwall test surface over about one period of pin-fin surface pattern. The white circular regions encircled by the dotted lines represent the locations of the pin bases. The results are given for $Re_H = 1.83 \times 10^4$ and $T_{0i}/T_w = 0.93$ and are obtained over a measurement area near the downstream portion of the test surface, which extends over X/D_h from 11.7 to 13.3. This is in the vicinity of pins in the 11th and 12th rows for the pin arrangement shown in Fig. 3. In Fig. 9, flow is directed from bottom to top in the increasing X/D_h direction. The data in Fig. 9 are time averaged using 25 instantaneous data sets acquired over a period of 25 s.

Figure 9 shows that local Nusselt number ratios Nu/Nu_0 are relatively low beneath the pin-fin wake (especially just downstream of each pin fin) because of a flow recirculation zone and relatively low velocities. Farther downstream, local Nusselt number ratios Nu/Nu_0 values increase to become greater than 2.2 as local flow velocities increase, and large-scale unsteadiness forms. These high Nusselt number ratio Nu/Nu_0 regions are evident in Fig. 9 at Z/D_h values less than -0.3, at Z/D_h values greater than $+0.3$, and at X/D_h values from 12.3 to 12.7. At the edges of the wakes, the shear layer enhances local surface Nusselt numbers along vertical strips over X/D_h from 11.8 to 12.7, which emanate from the spanwise edges of the pins near Z/D_h of -0.25 and $+0.25$. The most important mechanism for local heat transfer enhancement is the primary and secondary horseshoe vortices that form upstream of each pin fin at the pin–wall junction. The enhancement is a result of the secondary advection provided by these vortices as they advect away from the stagnation line located on the upstream pin-fin edge. The secondary advection rearranges cooler fluid, originally located from away from the test surface, so that it is in close proximity with the heated test surface. The resulting Nusselt number ratios Nu/Nu_0 augmentation is evident in Fig. 9 at Z/D_h from -0.3 to $+0.3$ and at X/D_h from 12.6 to 12.8.

Comparisons of Pin-Fin Heat Transfer and Friction Factor Data

In Fig. 10, results from different pin-fin investigations are compared in Nusselt number ratios $\overline{Nu}/Nu_0$ vs Reynolds number Re_d coordinates. This Reynolds number is based on pin-fin diameter d and the maximum velocity that exists at the location in the pin-fin array with the greatest blockage, where the cross-sectional area of the flow

is minimum, as suggested by Chyu.[14] The Nusselt number data in Fig. 10 are plotted as dependent on this parameter because data from Chyu,[14] Uzol and Camci,[22] and Ligrani and Mahmood[5] (for varying Reynolds number Re_d) for circular-staggered pin fins collect in one continuous distribution. This not only illustrates the agreement and consistency of these three different sets of heat transfer data, but also indicates the usefulness of this parameter in correlating heat transfer data from channels with pin fins. The circular-staggered pin-fin data from these different sources are then in approximate agreement with values from Chyu[14] for circular-in-line, fillet-cylinder-in-line, and fillet-cylinder-staggered types of pin fins, but are higher than elliptic pin-fin data (N fin and SEF) from Uzol and Camci.[22] Figure 10 also shows Nusselt number ratio $\overline{Nu}/Nu_0$ data from Ligrani and Mahmood,[5] which increase from 2.2 to 3.0 as the temperature ratio T_{0i}/T_w decreases from 0.93 to 0.68. Because of the effects of variable properties, these data are located above the circular-staggered pin-fin data obtained at different Reynolds numbers (and T_{0i}/T_w near 1.0).

Figure 11 compares globally averaged Nusselt number ratios and friction factor ratios from different pin-fin investigations.[5,14,20,21] The highest heat transfer and friction factor augmentations are produced by arrays of staggered cube pin fins[20] and staggered diamond pin fins.[20] Notice that these results are positioned near the top of a continuous band of data comprising results from Chyu,[14] Chyu et al.,[20] Hwang and Lu,[21] and Ligrani and Mahmood.[5] Differences between these different data sets are mostly a result of different Reynolds numbers, different arrangements of pin fins, and different pin-fin shapes. For example, the data obtained at lower Reynolds numbers[14,20,21] generally show decreasing Nusselt number ratios as the friction factor ratio increases. This trend is especially apparent for the circular-in-line and circular-staggered configurations from Chyu.[14] The data set obtained at higher Reynolds number from Ligrani and Mahmood[5] shows a different trend.

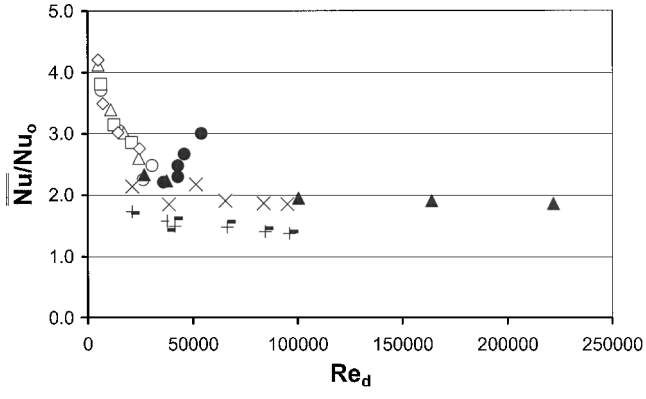

Fig. 10 Comparison of globally averaged Nusselt number ratios $\overline{Nu}/Nu_0$ as dependent on Reynolds number Re_d from different pin-fin investigations[5,14,22]: ○, circular, in-line[14]; △, circular, staggered[14]; □, fillet-cylinder, in-line[14]; ◇, fillet-cylinder, staggered[14]; ×, circular, staggered[22]; –, elliptic SEF, staggered[22]; +, elliptic N fin, staggered[22]; ●, circular, staggered, varying T_{0i}/T_w (Ref. 5); and ▲, circular, staggered, varying Reynolds number Re_d (Ref. 5).

Different thermal boundary conditions and differences in measurement approach may also account for relatively small variations between different data sets in Fig. 11. For example, Chyu[14] and Chyu et al.[20] employ the naphthalene-sublimation technique to measure mass transfer on pins and on endwalls, whereas the other investigations[5,21,22] measure Nusselt numbers only on endwalls. Except for the first one or two rows, Chyu et al.[16] indicate that heat transfer coefficients on circular pin surfaces are consistently higher than values on the endwall by 10–20%. Van Fossen[10] reports a 35% differential, whereas Al Dabagh and Andrews[25] report pin surface heat transfer coefficients that are 15–35% lower than endwall values. Chyu et al.[16] further indicate that array-averaged results, such as the ones shown in Fig. 11, are "virtually equal to corresponding endwall averages" largely because the endwall often accounts for the majority of the total wetted area.

Dimpled Surfaces

Dimples are arrays of indentations along surfaces. These are often spherical in shape, although a variety of other shapes have also been employed, ranging from triangular to tear drop. These are an attractive method for internal cooling because they produce multiple vortex pairs that augment local Nusselt number distributions as they advect downstream. They are notable for the low-pressure drop penalties that they produce, which is because they do not protrude into the flow to produce significant amounts of form drag. With this benefit, dimples offer advantages for cooling later turbine stages where lower pressure cooling air is employed. They are also advantageous because the pressure drop that they produce through an airfoil passage is relatively low, which allows favorable pressure margins to be maintained in other parts of the airfoil interior.

The first known published studies of the effects of hemispherical dimples on the flow structure and heat transfer characteristics are of Russian origin. Of these, Murzin et al.[26] describe the flow over and within shallow spherical depressions and conclude that this flow is mostly symmetric and consists of a stable recirculatory flow inside of the depression. Streamlines were observed to wind around a horseshoe-shaped vortex line and to form a helical pattern. In addition, "the pressure gradient due to rotation creates an outflow along the rotation axis and an inflow of liquid toward it in the boundary layer."[26] Gromov et al.[27] describe symmetric and nonsymmetric streamlines and flow patterns produced by hemispherical cavities with a variety of sizes. Cells of fluid motion are described in the form of tightening spirals, helical streamlines, and horseshoe-shaped vortices. Kesarev and Kozlov[28] present distributions of local heat transfer coefficients inside of a single hemispherical cavity and indicate that the convective heat transfer from the cavity is higher, especially on the downstream portion, than that from the surface of a plane circle of the same diameter as the cavity diameter. The authors

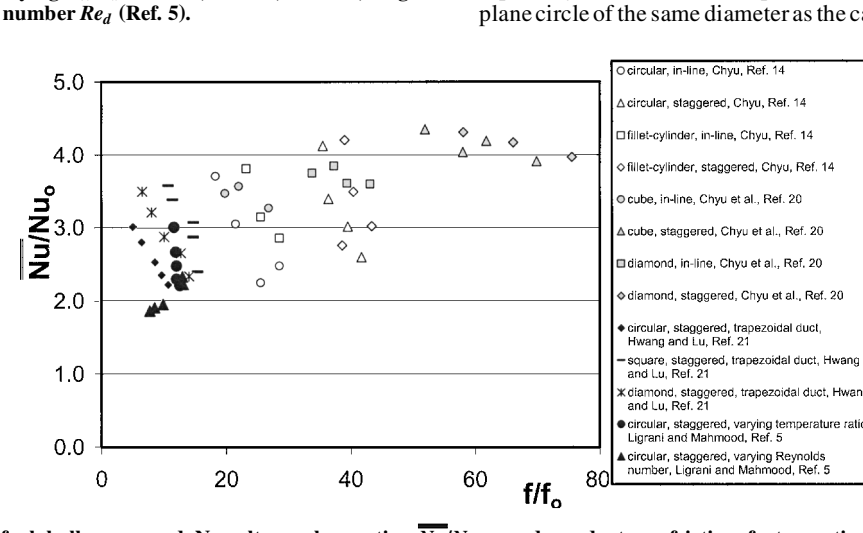

Fig. 11 Comparison of globally averaged Nusselt number ratios $\overline{Nu}/Nu_0$ as dependent on friction factor ratio f/f_0 from different pin-fin investigations.[5,14,20,21]

also describe the effects of turbulence intensity of the incident flow on the local heat flux and on the local shear stress on the cavity surface. According to the authors, the heat transfer from the hemispherical cavity is enhanced as the turbulence intensity increases.

Afanasyev et al.[29] describe the heat transfer enhancement mechanism for flows over walls indented with regular arrays of spherical pits with several different shapes. The dynamic and thermal properties of the boundary layer on the smooth surface between the pits is considered. Enhancements of 30–40%, with pressure losses that are not increased appreciably relative to a smooth surface, are reported. The authors also indicate that cavity shape does not have a significant effect on local flow hydrodynamics. Belen'kiy et al.[30] describe heat transfer intensification from a tube surface fitted with a staggered array of concave dimples on surfaces annular internal passages. Results, applicable to shell-and-tube heat exchangers, show maximum relative increases in overall heat transfer for deep cavities of about 2.5 and for shallow cavities of about 2.0, compared with smooth annular internal passages. In some cases, high-pressure losses are reported; however, in others, heat transfer enhancements are accompanied by decreases in pressure loss.

Terekhov et al.[31] present experimental measurements of flow structure, pressure fields, and heat transfer in a channel with a single dimple on one surface. Different magnitudes and frequencies of flow oscillations are described, along with heat transfer and pressure loss dependence on dimple geometry. According to the authors, "auto oscillations" of the flow arise in the cavity for all experimental conditions tested. Pressure losses increase (compared to a smooth wall) with an increase of cavity depth and decrease as the Reynolds number increases. Cavity heat transfer enhancements are also noted, especially for shallow holes, mainly as a result of an increase in heat transfer area and the changes to flow structure produced by the dimple. From flow visualizations, Zhak[32] describes a variety of vortex structures in different shaped rectangular cavities. Schukin et al.[33] present results that are directly applicable to gas turbine cooling. Average heat transfer coefficients are reported from the measurements on a heated plate downstream of a single hemispherical cavity in a diffuser channel and in a convergent channel. The study provides data on the influences of the mainstream turbulence intensity level and the angles of divergence and convergence on heat transfer augmentation. The authors conclude that heat transfer is augmented using a cavity in flows with either positive or negative pressure gradients. The authors also observe that the heat transfer from the inner surface of a cavity depends on the mainstream turbulence level.

In the early 1990s, several dimple investigations are reported, which originate from sources outside of Russia. One of the earliest of these is described by Bearman and Harvey,[34] who investigate crossflows over cylindrical surfaces with an array of dimples. The geometry of the dimples corresponds to the optimum concavity depth found by Kimura and Tsutahara[35] for minimum drag on cylinders. At high Reynolds numbers, significantly lower drag coefficients are present with arrays of dimples compared to smooth surfaces. Kithcart and Klett[36] compare heat transfer and skin friction of flows over surfaces on one wall of a rectangular channel with hemispherical dimples, hemispherical protrusions, and rectangular protrusions. The authors conclude that all three geometries produce similar levels of heat transfer augmentation. However, the level of skin friction varies considerably with geometry, since "hemispherical dimples significantly augment heat transfer with a lower penalty in increased skin friction relative to protrusion roughness."[36]

More recently, Chyu et al.[37] present data showing the effects of Reynolds number on local heat transfer coefficient distributions on surfaces imprinted with staggered arrays of two different shapes of concavities: spherical and tear drop. Their measurements, for ratios of channel height to dimple print diameter of 0.5, 1.5, and 3.0, show distributions of heat transfer coefficients everywhere on surfaces that are significantly higher than values in channels with smooth surfaces. Over a range of Reynolds numbers, enhancement of the overall heat transfer rate is about 2.5 times smooth surface values, and friction factors are about half the values produced by conventional rib turbulators. Of the two dimple shapes considered, the tear drop generally induces somewhat higher surface heat transfer, especially when applied to opposite walls of the rectangular channel. Lin et al.[38] present computational simulation results of the flow structure and resulting heat transfer distributions for the same surface geometries and flow conditions. Flow streamlines and temperature distributions are presented that provide insight into the flow structural characteristics produced by the dimples. According to the authors, two vortical structures form as the flow enters each dimple. In addition, surface heat transfer rates generally increase when dimples are placed symmetrically on two opposite walls and the walls are brought closer together. Another study, described by Gortyshov et al.,[39] employs spherically shaped dimples, called spherical intensifiers, placed at different relative positions on the opposite sides of a narrow channel. The investigators observe that an increase in relative dimple depth produces increases in surface heat transfer rates, as well as increases in streamwise pressure penalties. When dimples are used on two sides of channel, flow structures produced by each side interact with each other in a nonlinear fashion, with net behavior that cannot be determined using superposition. Moon et al.[40] give heat transfer and friction factor data, for ratios of channel height to dimple print diameter from 0.37 to 1.49, that illustrate the effects of channel height on a surface with a staggered pattern of dimples. According to these investigators, improvements in heat transfer intensification and pressure losses remain at approximately constant levels over the ranges of Reynolds number and channel height investigated.

Another recent study by Syred et al.[41] considers a single dimple on the concave or convex surface of a rectangular cross section channel. The dimple geometry and passage height are held constant, as the Reynolds number and amount of curvature are varied. According to the authors, the turbulent fluctuations in the dimple on the concave surface exceed those in a dimple placed on a convex surface. In addition, surface heat transfer rates in the dimple increase when the dimple is located on a concave surface and decrease when placed on a convex surface, relative to values measured on smooth surfaces. Chen et al.[42] employ hemispherical protrusions on the insides of tubes to augment surface heat transfer rates. Six different protrusion arrangements are employed, which increase surface heat transfer rates above those present in smooth tubes by 25–137% when compared at the same Reynolds number. With such improvements, the authors[42] indicate that the size and weight of coaxial-pipe heat exchangers can be reduced "by a factor of almost 2."

From work conducted at the University of Utah, Mahmood et al.[43] describe the mechanisms responsible for local- and spatially averaged heat transfer augmentations on flat channel surfaces with an array of dimples along one wall. In this study, the ratio of channel height to dimple print diameter is 0.5. The most important mechanisms are 1) the reattachment of the shear layer that forms across the top of each dimple, 2) the vortex structures and vortical fluid shed from each individual dimple indentation, which then advect over the flat surface just downstream, and 3) the periodic unsteadiness, which is produced as flow is ejected and then inrushes to each dimple. These different effects result in increased advection due to secondary fluid motions, as well as increased turbulence transport levels in the flow near the dimples. The authors also indicate that the effects of the vortex structures are particularly pronounced near the downstream rims of each dimple. The resulting high local Nusselt number regions on the flat surface are spread over a region that is approximately parallel to the downstream edge of each dimple and along two strips of flat surface located near the spanwise edges of downstream-diagonal adjoining dimples. These augmented regions are spread over larger surface areas and become more significant as the ratio of inlet stagnation temperature to local surface temperature decreases. In another paper, Mahmood and Ligrani[44] consider the effects of the ratio of inlet stagnation temperature to local surface temperature for ratios of channel height to dimple print diameter of 0.20, 0.25, 0.50, and 1.00. According to these authors, visualized smoke patterns show that vortex pairs, which are periodically shed from the dimples, become stronger as the ratio of channel height to print diameter decreases. However, regardless of the ratio of channel height to dimple print diameter, local Nusselt numbers increase substantially as the ratio of inlet stagnation temperature to local surface temperature decreases. Additional information on the flow structure due to dimple depressions on a channel surface is

provided by Ligrani et al.[45] Detailed descriptions of the behavior of the primary and secondary vortex pairs, which are shed from the dimples, are described. Most important, the locations of the primary and secondary vortex pairs coincide closely with locations where the normalized longitudinal Reynolds normal stress is increased. Frequent, continuous, unsteady interactions are also described between the flows in adjacent dimples, where the frequency of the large-scale unsteadiness scales on time-averaged bulk velocity and dimple print diameter.

Mahmood et al.[46] and Ligrani et al.[47] consider heat transfer and flow structure in a channel with dimples and protrusions on opposite walls. Similar arrangements, but only with measurements of friction factors and some flow structural characteristics, are considered by Kithcart and Klett.[36] According to Ligrani et al.,[47] instantaneous flow visualization images and surveys of time-averaged flow structure show that the protrusions result in added vortical, secondary flow structures and flow mixing. As a result, local friction factors and local Nusselt numbers are augmented compared to a channel with no protrusions on the top wall. Mahmood et al.[46] indicate that important Nusselt number variations are observed as the array of protrusions is changed with respect to the locations of the dimples. With protrusions, form drag and channel friction are increased. As a result, thermal performance parameters are then generally slightly lower when protrusions and dimples are employed, compared to a channel with a smooth-dimple arrangement.

Dimple Surface Flow Structure

Figure 12 shows a flow cross section (or spanwise-normal plane) visualized using smoke generated from multiple smoke wires, at a Reynolds number based on channel height of 1.25×10^3 from Ligrani et al.[45] These data are obtained just downstream of a dimple located in the ninth row of a test surface, shown in Fig. 13 (all dimensions in centimeters), installed on the bottom surface of a channel. Note that this flow visualization plane is then located between two dimples located in the 10th row. The ratio of channel height to dimple print diameter is 0.50, and the ratio of dimple depth to dimple print diameter is 0.2. The image in Fig. 12 shows a primary vortex pair located centrally in the image, which is positioned just downstream of the central part of the dimple located just upstream in the ninth row. This primary vortex pair is evidenced by a mushroom-shaped pattern, which is often often symmetric with respect to the centerline-normal plane and located above an upwash region. Two additional secondary vortex pairs and associated upwash regions are positioned on each side of the primary vortex pair (near the left and right spanwise edges of dimples in the 10th row). These are generally near diagonal dimple locations, or just downstream of these locations.

The formation and ejection of these vortex pairs occur periodically.[31,43–45] During ejections, the flow from the central portion of the dimple moves upward with downward flow on either side to satisfy continuity. The outward motion from within the dimple (or upwash region) is quite strong, and when present at intermittent, periodic times, is oriented in a streamwise-normal plane roughly down the centerline of each dimple. The three-dimensional shapes

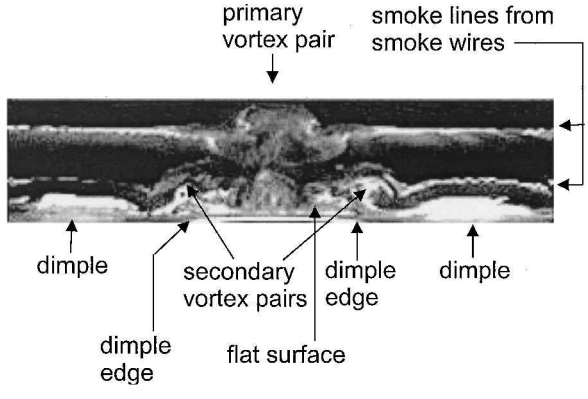

Fig. 12 Instantaneous flow visualization image for $Re_H = 1.25 \times 10^3$, from Ligrani et al.[45]: ratio of channel height to dimple print diameter is 0.5 and ratio of dimple depth to dimple print diameter is 0.2.

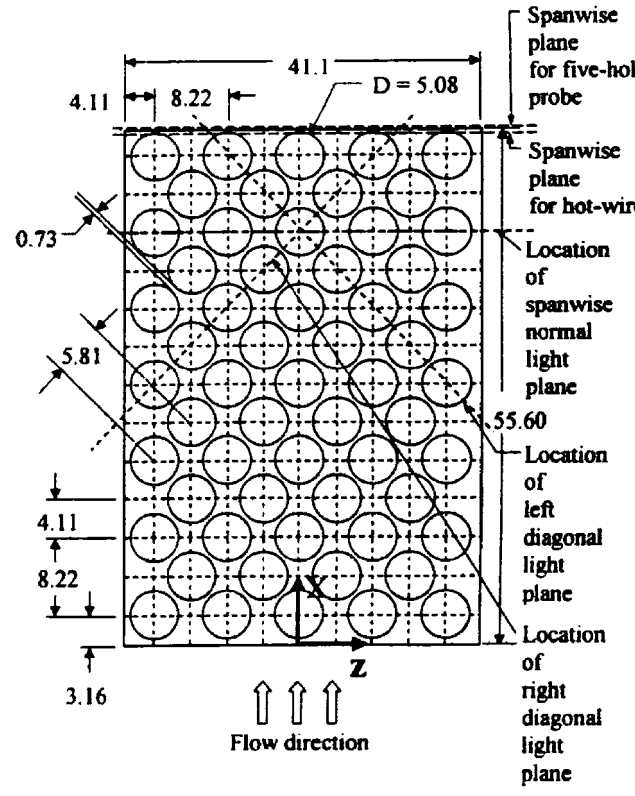

Fig. 13 Schematic diagrams from Ligrani et al.[45] All dimensions are given in centimeters.

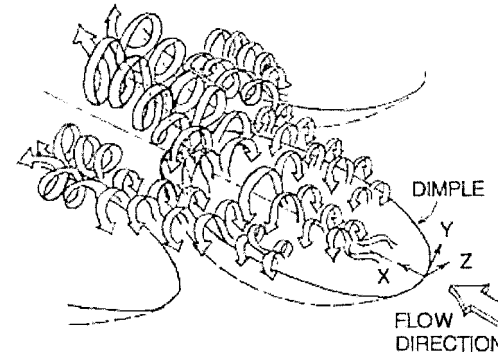

Fig. 14 Schematic diagram of instantaneous, three-dimensional flow structure corresponding to flow visualization image shown in Fig. 12; from Mahmood et al.[43]

of these vortex pairs are then illustrated in Fig. 14, which shows that the primary vortex pair is eventually stretched as it is advected downstream (by the streamwise bulk flow above the dimple horizon), becoming smaller in cross section and more elongated. The periodicity associated with shedding of packets of vortical fluid from individual dimples is, thus, an important feature of the flow structure produced by the dimpled surface. This occurs such that a packet of vortical fluid is shed, followed by an inrush of flow into the dimple, followed by another shedding event, and so on. The inward advection and outward shedding must both take place (either simultaneously or alternatively) if continuity is to be satisfied for the flow near the dimpled surface.

The two secondary vortex pairs near dimple diagonals, which are shown in Figs. 12 and 14, are often in the form of collections of

vortex pairs, or sometimes, short "braids" of vortical fluid. Because secondary pair formation is tied to flow behavior near sharp dimple edges (and because the dimples are placed on the surface in a staggered array), one secondary vortex pair is then in close proximity to the spanwise edges of many dimples as it advects downstream. These secondary vortex pairs are then steadier, with less position and location timewise variations, compared to the primary vortex pair shed from each dimple. The secondary flows within these secondary vortex pair structures often periodically impact on flat surfaces adjacent to dimples. These packets of vortical fluid are stretched farther from the dimple edges (especially in dimple diagonal directions) as the Reynolds number increases. This causes the braids of vortical fluid to advect just above and into the dimple volumes that are located diagonal and adjacent to the dimple responsible for the initial upwash of fluid. Such advection of vortical fluid from one dimple to another then contributes to the dynamic pressure behavior in adjacent dimples, and probably, the triggering of inrushes of fluid into adjacent dimples. Periodic impacting of such vortical fluid, which alternates with the periodic influx of bulk fluid, also helps augment turbulence transport levels in fluid at and near these dimpled surface locations. From the results in Figs. 12 and 14, it is evident that the axis of each vortex in each pair, after it is formed and advected some distance, is roughly longitudinal. The axes of rotation, orientations, locations, and structure of these vortices are about the same during different shedding events at a particular streamwise location.

From time-varying images, it is apparent that the vortical fluid is shed simultaneously with fluid shed from other dimples in the same streamwise row, but out of phase with the packets of fluid shed from dimples in an adjacent upstream or downstream dimple rows. This further evidences the strongly elliptic nature of the flow over the dimpled surface. Pressure variations in one dimple are believed to affect pressure variations in other, adjacent dimples (especially along dimple diagonals). The periodicity in this unsteadiness is well defined and does not seem to vary greatly in its frequency along a given dimpled surface at a particular flow condition, provided the flow is fully developed or nearly fully developed. Appropriate scaling parameters for the shedding frequency of the primary vortex pair seem to be time-averaged bulk velocity and dimple print diameter, which then gives $2\pi fD/\bar{U}$ of 1.7–1.8 for hemispherical dimples with a depth to print diameter ratio of 0.1. Magnitudes of this nondimensional frequency change with Reynolds number, streamwise location, as well as with dimple shape, spacing, and depth.

Figure 15 from Isaev et al.[48] shows that the flow inside of a spherical indentation dimple is also quite complex. These results are obtained from computer visualizations obtained by numerically solving the Reynolds equations. Isolines of the transverse flow velocity component are shown within the dimple and in the median cross section in Figs. 15a and 15b, respectively. Velocity vectors from the median cross section are shown in Fig. 15c. Even though the dimple is symmetric, nonsymmetric flow patterns are evident within the dimple. In the cross-sectional views, "two large-scale vortex cells" are evident. According to the investigators,[48] "large-scale vortex rings, inside which particles perform reciprocating motions, are incorporated into the spiral flows outgoing from singularities at the surface of the well."

Time-averaged flow structure also provides insight into the behavior of flows above dimpled surfaces. Surveys of time-averaged streamwise vorticity, obtained from measurements made just downstream of 13 rows of dimples, are given in Fig. 16 for a ratio of channel height to dimple print diameter of 0.50 and a Reynolds number based on channel height $Re_H = 9.4 \times 10^3$. The ratio of dimple depth to dimple print diameter is 0.2. Note that bulk flow direction is into the plane of the paper of each contour plot, the dimples are located at the bottom of each plot, and all data are normalized.

In Fig. 16, positive and negative regions of vorticity, associated with the primary vortex pair and seen earlier in flow visualization results, are readily apparent. In the time-averaged flowfield, the two vortices in this pair are located on either side of the upwash region located near $Z/H = 0$. Four other smaller and weaker regions of positive and negative vorticity (in two pairs) are also apparent in Fig. 16 nearby the regions containing the primary vorticity. Two

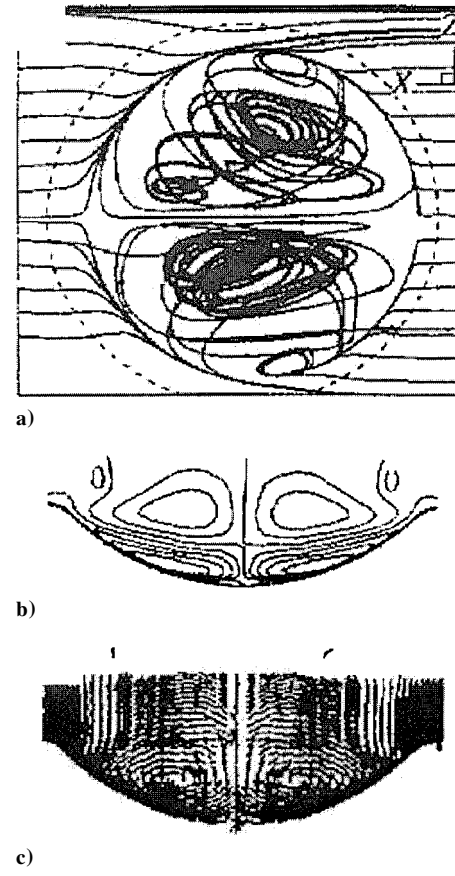

Fig. 15 Numerically predicted flow characteristics within and near a symmetric, spherical indentation dimple; from Isaev et al.[48]: a) isolines of transverse flow velocity component within a dimple, b) isolines of transverse flow velocity component in median cross section of a dimple, and c) velocity vectors from the median cross section.

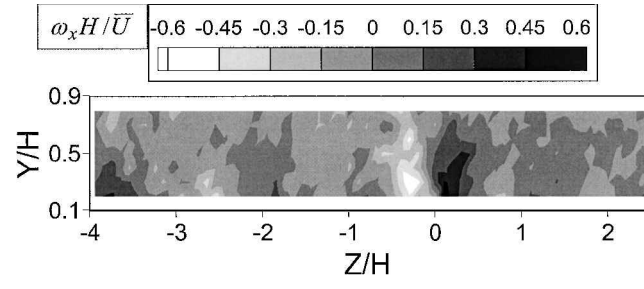

Fig. 16 Survey of nondimensional streamwise vorticity $\omega_x H/\bar{U}$ measured just downstream of the test surface shown in Fig. 13 for $Re_H = 9.4 \times 10^3$.

of these are located near the smooth wall, located opposite to the dimpled surface, and two are located just to the sides of the primary vortex pair, but nearer to the dimpled wall at $Y/H = 0.2$–0.3. These latter regions are a consequence of the secondary vortex pairs also observed in flow visualization images near dimple edges. Also evident on the vorticity contours in Fig. 16 are the fairly large regions of relatively weak positive and negative vorticity that are centered around $Z/H = -2.2$. These are located just downstream of dimple centerlines in the next to last row (or 12th streamwise row). As a result, these vorticity regions are much weaker than the ones located immediately downstream of dimples in the 13th streamwise row.

Key flow features responsible for local heat transfer augmentations include 1) shedding of multiple vortex pairs from dimples, 2) strong secondary fluid motions within these vortex pairs and associated vortical fluid, 3) shear layer reattachment within each dimple, and 4) periodicity and unsteadiness associated with vortex pair shedding and the flows within individual dimples. This unsteadiness

causes the thermal boundary layer that forms downstream of individual dimples to be periodically reinitialized and increases flow mixing over length scales approximately equal to the dimple print diameter. The effects on thermal transport are especially pronounced near downstream rims of dimples as well as on flat surfaces downstream of and between dimples.

Example of Spatially Resolved Surface Nusselt Number Distribution

Figure 17 presents spatially resolved Nusselt numbers from Burgess et al.[49] measured on the dimpled test surface placed on one wall of a channel with a height to dimple print diameter ratio of 1.0 and a ratio of dimple depth to dimple print diameter of 0.2.

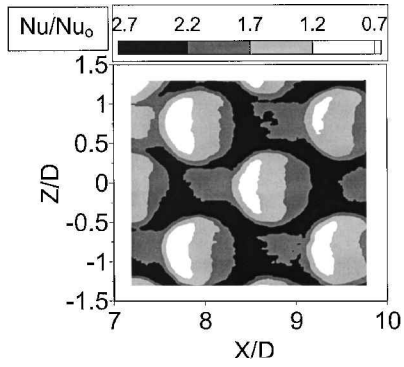

Fig. 17 Local Nusselt number ratio data from a channel with dimples and heating on one channel surface for $Re_H = 2.0 \times 10^4$; from Burgess et al.[49]

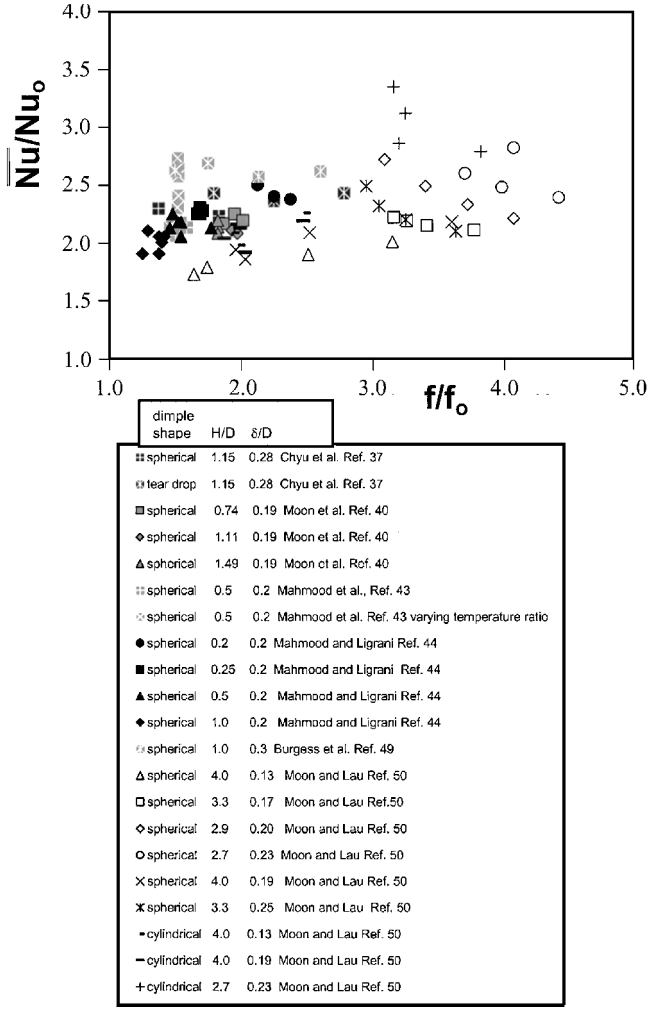

Fig. 18 Comparison of globally averaged Nusselt number ratios $\overline{Nu}/Nu_0$ as dependent on friction factor ratio f/f_0 from different dimpled surface investigations[37,40,43,44,49,50]: all data for smooth top wall and dimpled bottom wall.

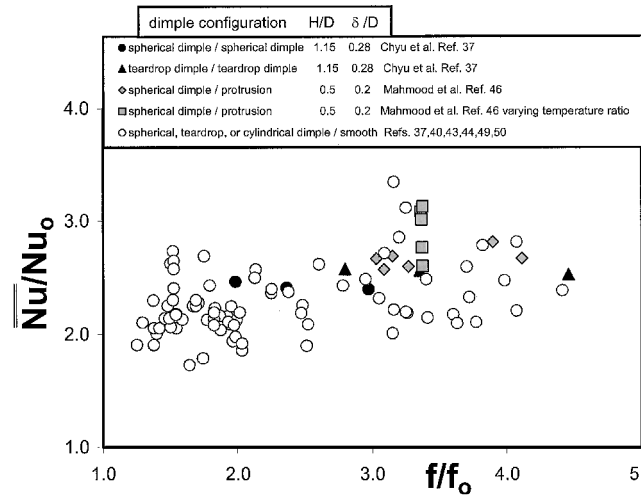

Fig. 19 Comparison of globally averaged Nusselt number ratios $\overline{Nu}/Nu_0$ as dependent on friction factor ratio f/f_0 from different investigations: data for a smooth top wall and a dimpled bottom wall,[37,40,43,44,49,50] for dimples on both top and bottom walls,[37] and for dimples on one wall with protrusions on the opposite wall.[46]

The opposite channel wall is smooth. Reynolds number based on channel height for the measurements is 2×10^4. Flow direction for Fig. 17 is from top to bottom in the direction of increasing X/D. The image shows dimples in the 10th–12th rows from the beginning of the test surface shown in Fig. 13.

The locations of the circular concave depressions of the dimples correspond to circular Nusselt number ratio Nu/Nu_0 contours in Fig. 17. Lower Nusselt number ratios are located over the upstream halves of the depressions. Local Nusselt number ratios are then higher in the downstream halves. The highest values are then located near the downstream rims of each dimple, both slightly within each depression, and on the flat surface just downstream of each dimple. Consistent with the results of Kesarev and Kozlov[28] and Schukin et al.,[33] most local values in the concave cavities are higher than values measured a smooth channel at the same Reynolds number and temperature ratio.

Referring to the area over Z/D from -0.3 to $+0.3$, and over X/D from 9.1 to 9.7, the high Nusselt number ratio Nu/Nu_0 region is spread over a region that is approximately parallel to the downstream edge of the dimple. Two "fingers" from this region then extend downward in the positive X/D direction, which are located near the spanwise edges of adjoining dimples. These fingers continue to extend downward in the $+X/D$ direction until they connect with high Nusselt number ratio Nu/Nu_0 regions located on the flat surfaces just downstream of the adjacent dimples. These fingers are due to the edge or secondary vortex pairs, which strengthen as they advect downstream next to the edges of other dimples. This occurs because of the staggered arrangement of the dimples on the test surface, which causes each "edge" vortex pair to be located first on the right edge of a dimple, then on the left edge of another dimple, and so on. The result is interconnected regions of high local Nusselt number ratios, located to the sides of and diagonally between dimples in adjacent rows, as shown in Fig. 17.

Comparisons of Dimpled Surface Heat Transfer and Friction Factor Data

Figures 18 and 19 present data from channels with dimple–smooth arrangements,[37,40,43,44,49,50] dimple–dimple arrangements,[37] and dimple–protrusion arrangements[46,47] (where each of these denotes the surface types on opposite sides of a large aspect ratio channel). All of the data in Figs. 18 and 19 are based on heat fluxes deduced using flat, projected areas. As mentioned earlier, dimpled surfaces generally produce lower friction factors compared to the several other types of heat transfer augmentation devices.

All of the data presented in Fig. 18 are obtained with dimples on one wall of the channel only, with smooth surfaces on all other channel walls. Data from Chyu et al.,[37] Moon et al.,[40] Mahmood

et al.,[43] Mahmood and Ligrani,[44] and Burgess et al.[49] collect on one continuous distribution with Nusselt number ratios $\overline{Nu}/Nu_0$ ranging from 1.8 to 2.8, and f/f_0 ranging from 1.3 to 2.9. The highest Nusselt number augmentations are produced by spherical indentation dimples with $\delta/D = 0.3$ (Ref. 49). Data from Moon and Lau[50] cover about the same range of Nusselt number ratios as the other data sets. The baseline Nusselt number Nu_0 values used for normalization of the Moon and Lau data are based on recommendations made by these authors.[50] Friction factor ratios from Moon and Lau[50] are, in some cases, higher than values from these other sources.[37,40,43,44,49] Note that the Moon and Lau[50] results are based on measurements made only at a few discrete locations on their test surface, whereas the other studies obtained results from averages made from spatially resolved results, measured over continuous sections of test surfaces. Other differences between the different data sets are due to different Reynolds numbers, different dimple spacings, different channel turbulence intensities, and differences in other parameters employed.

In Fig. 19, the highest levels of heat transfer augmentation are obtained using dimples and protrusions, aligned with each other on opposite sides of the channel.[46] Notice that Nusselt number ratio $\overline{Nu}/Nu_0$ values for this arrangement increase continuously at one f/f_0 value as the ratio inlet stagnation temperature to local wall temperature decreases.[46] The highest friction factors are produced using a tear-drop-shaped dimple–dimple configuration,[37] that is, tear-drop-shaped dimples on opposite sides of the channel. Different dimple–smooth configurations then generally yield comparatively lower values of heat transfer augmentation and friction factor ratios in Fig. 19.

Rib Turbulators

Rib turbulators are often in the form of rectangular cross-sectional bars mounted along the surface, which are often angled with respect to the bulk flow direction. Because they protrude into the flow, they act to trip the flow, mix the flow, and also generate vortices and three-dimensional velocity gradients. Typical arrangements are shown in Figs. 20, 21c, and 22a. Rib turbulators, or trip strips, are general-purpose heat transfer augmentors in cooled airfoils. When the main geometric parameters, trip strip height, channel blockage, orientation, and spacing, are varied, it is possible to optimize the cooling scheme in such a way that the airfoil midbody is not overcooled, while providing the necessary exit temperatures at the leading edge and trailing edge, where film cooling may be required.

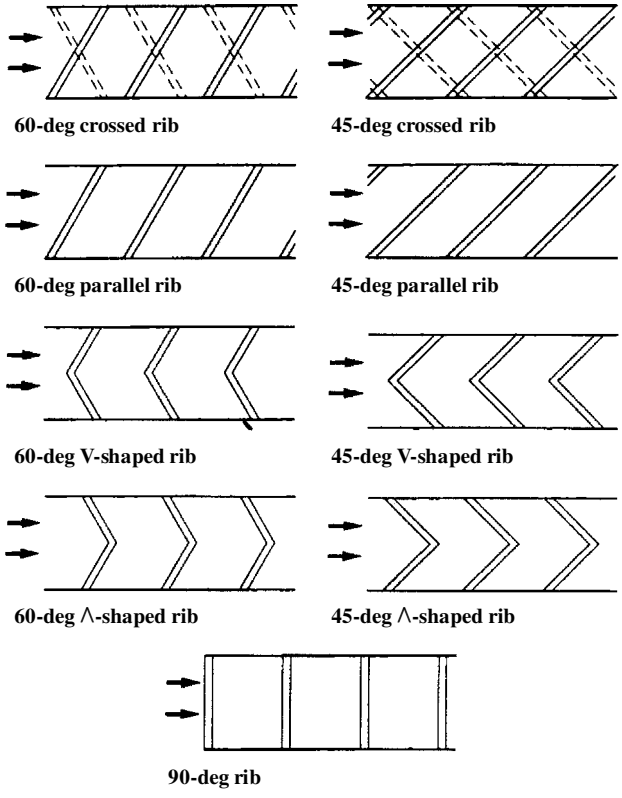

Fig. 20 Rib turbulator configurations (top views); from Han et al.[53]

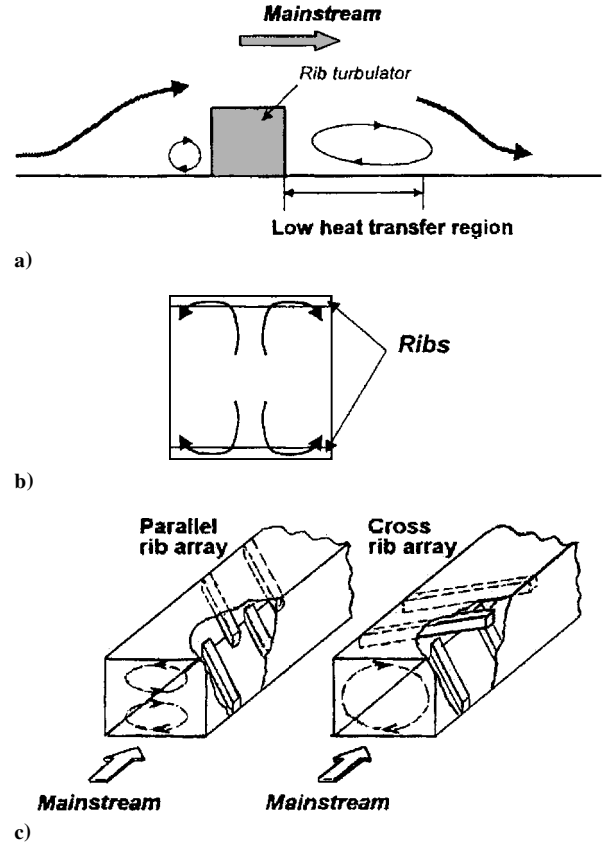

Fig. 21 Schematic diagrams of flow patterns in ducts with rib turbulators from Cho et al.[61]: a) flow recirculation patterns around a single rib, b) weak secondary flows downstream of the reattachment line induced by noncircular duct geometry for 90-deg rib turbulators, and c) strong secondary flows induced by rib turbulators angled at 45 deg.

A significant number of experimental and numerical studies address the effects of rib turbulators on heat transfer in internal channels.[51–97] Considered are single-pass and multipass channels, square and rectangular channels, channels with and without rotation, and rotating channels with different orientations with respect to the axis of rotation.

Several of the earliest experimental studies consider single-pass, stationary channels with no rotation. Of these studies, Han et al.[51] address the effects of rib shape, angle of attack, and pitch to height ratio. According to these investigators, ribs with 45-deg inclinations produce better heat transfer performance than ribs with 90-deg orientations, when compared at the same friction power. Han and Park[52] vary the channel aspect ratio and conclude that the best heat transfer performance is obtained using a square channel with a rib turbulator angle of attack from 30 to 45 deg. This range of angles of attack also yield the best heat transfer performance for rectangular channels. However, the overall performance of square channels is superior to rectangular channels. Both Nusselt number ratio Nu/Nu_0 data and f/f_0 data are presented. Han et al.[53] indicate that best heat transfer enhancements in square channels are produced by V-shaped ribs with 45- and 60-deg arrangements, followed by 45- and 60-deg parallel ribs, which are followed by 45- and 60-deg crossed ribs. Han et al.[54] also provide both Nusselt number ratio Nu/Nu_0 data and f/f_0 data. These individuals investigate wedge-shaped and delta-shaped turbulence promoters in square channels and compare their performance with existing data for different types of rib turbulators. Delta-shaped ribs generally perform better than the wedge-shaped ribs, especially when the delta-shaped ribs on opposite walls are aligned and arranged with a backward flow direction. The investigators also indicate that broken configurations of delta-shaped ribs and wedge-shaped ribs both give better performance than full-length

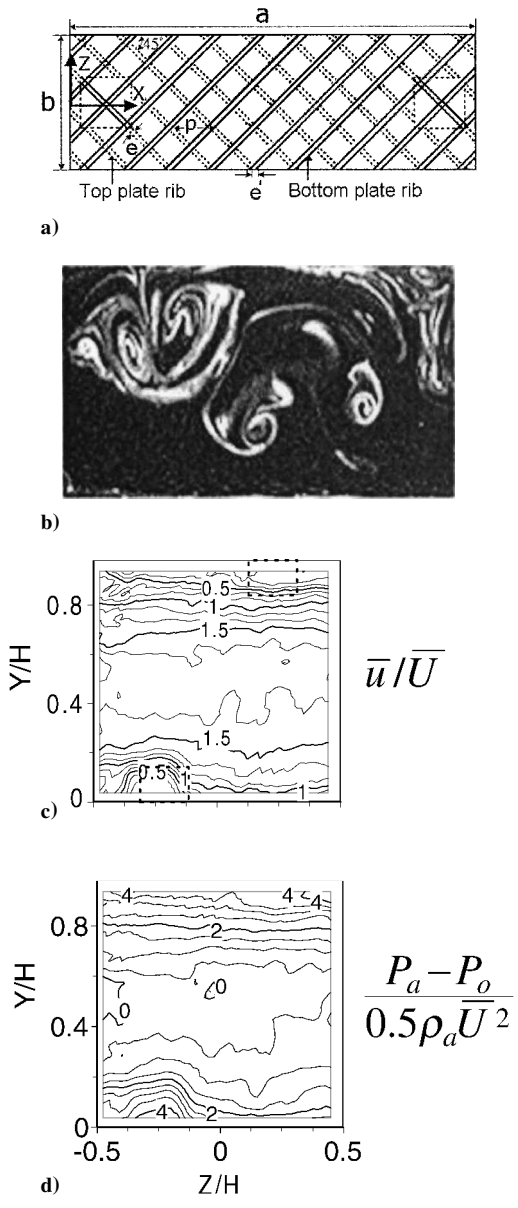

Fig. 22 Rib turbulator flow structure: a) schematic diagram of the rib turbulator test surfaces with 45-deg rib turbulators, b = 411.0 mm, a = 1232.9 mm, p = 128.4 mm, e = 12.8 mm, and e' = 18.2 mm with flow direction left to right; b) instantaneous flow visualization image illuminated in a spanwise-normal plane downstream of the rib turbulator test section at X = 1462 mm for Re_H = 430; c) time-averaged survey of local streamwise velocity in a spanwise-normal plane located just downstream of the rib turbulator test section at X = 1235 mm for $Re_H = 8 \times 10^3$; and d) time-averaged survey of local total pressure in a spanwise-normal plane located just downstream of the rib turbulator test section at X = 1235 mm for $Re_H = 8 \times 10^3$.

configurations. Taslim et al.[55] provide additional evidence that 45-deg ribs produce higher thermal performance factors than 90-deg ribs. The authors also indicate that, of the configurations examined, the highest heat transfer enhancements and highest friction factors are produced by low-blockage ratio V-shaped ribs. In a later study, Taslim et al.[56] study 12 different geometries of ribs that are placed on all 4 walls of channels with both square and trapezoidal cross sections. Compared to channels with ribs on two walls, heat transfer coefficients and thermal performance factors are enhanced. More recently, Casarsa et al.[57] characterize the velocity and heat transfer fields in an internal cooling channel with 90-deg ribs that produce 30% blockage. Included are heat transfer enhancement magnitudes, time-averaged distributions of mean velocity components, and time-averaged distributions of normalized root-mean-square velocity fluctuations. Ligrani and Mahmood[58] present spatially resolved Nusselt numbers and friction factors for a stationary channel with an aspect ratio of 4 and angled rib turbulators inclined at 45 deg with perpendicular orientations on two opposite surfaces. The ratio of rib height to hydraulic diameter is 0.078, the rib pitch-to-height ratio is 10, and the blockage provided by the ribs is 25% of the channel cross-sectional area. According to these authors, spatially resolved local Nusselt numbers are highest on tops of the rib turbulators, with lower magnitudes on flat surfaces between the ribs, where regions of flow separation and shear layer reattachment have pronounced influences on local surface heat transfer behavior. Also included are data corrected to account for three-dimensional conduction within the ribbed test surface.

Other recent studies of stationary channels with no rotation consider single-pass and multipass channels. Wang et al.[59] present heat transfer results from square ducts with 45-deg ribs. Thurman and Poinsatte[60] measure heat transfer and bulk air temperature in a three-pass duct with orthogonal ribs and bleed holes both located on one wall. According to these investigators, changing the locations of the ribs relative to the holes produces large changes to surface heat transfer coefficient distributions. Cho et al.[61] employ continuous and discrete, parallel and cross arrays of ribs in a single-pass square duct. Discrete ribs with gaps in between are found to produce more uniform heat transfer coefficient distributions than continuous ribs.

Other recent experimental studies investigate heat transfer in channels with rotation and square cross section. Of these studies, Johnson et al.[62] and Fan et al.[63] examine four-pass serpentine channels and indicate that the best performance is produced by ribs with 45-deg arrangements. Parsons et al.,[64] Johnson et al.,[65] Zhang et al.,[66] Parsons et al.,[67] and Dutta and Han[68] consider two-pass channels with different rib turbulator configurations. Three of these studies[65,67,68] also consider the influences of changing the channel orientation with respect to the axis of rotation. Heat transfer data are presented that show that the influences of Coriolis forces and crossstream flows decrease as channel orientation changes from normal to angled. Another pair of studies by Park et al.[69,70] consider the effects of rib size on local heat transfer coefficients with radially outward flow and transverse ribs on the trailing and leading walls of an internal passage.

Experimental heat transfer studies using channels with rotation and rectangular cross section are less numerous. Of studies in this area, Taslim et al.[71,72] employ single-pass channels with orthogonal rotation and either staggered transverse ribs[71] or 45-deg ribs arranged with perpendicular orientations on opposite channel walls.[72] In both cases, more pronounced rotation effects are evidenced as the channel aspect ratio increases, or as the rib blockage ratio decreases. Azad et al.[73] employ a two-pass channel with rib turbulators on leading and trailing sides at angles of 45 deg with respect to the mainstream flow. Rotating rib wall heat transfer coefficients are two to three times values measured on rotating smooth walls. Heat transfer coefficients on the first-pass trailing side and second-pass leading side are enhanced by rotation, whereas the first-pass leading side and second-pass trailing side values are diminished by rotation. In addition, 45-deg ribs that are parallel on opposite channel walls produce higher augmentations than 45-deg ribs which are perpendicular on opposite channel walls. Griffith et al.[74] examine rotation effects in a channel with an aspect ratio of 4 and 45-deg angled ribs placed on two opposite walls. According to these investigators, higher heat transfer enhancements are present compared to square channels and channels with an aspect ratio of 2. Nusselt number augmentations change significantly on the ribbed leading surface and smooth side surfaces as the duct orientation with respect to rotation direction is altered. Augmentations on the ribbed trailing surface and smooth side surfaces exhibit a strong dependence on rotation number.

An experimental and numerical investigation by Dutta et al.[75] examines the effects of rib turbulators on heat transfer behavior in a rotating, two-pass channel with a triangular cross section. Two channel orientations with respect to the axis of rotation are considered, along with the effects of channel orientation on secondary flows. Liou et al.[76] present heat transfer, fluid flow, and pressure measurements made in a rotating two-pass, square duct with 90-deg ribs positioned near the leading and trailing surfaces. The ribs are

arranged so that they are detached from the leading and trailing surfaces, which results in more uniform heat transfer distributions compared to attached ribs. Rib detachment also gives enhanced heat transfer on the leading surfaces of the first outward pass and on the trailing surface of the second inward pass, compared to similar channels with attached ribs. Bunker et al.[77] describe experimental results from an investigation of a complex trailing edge passage for a high-pressure turbine blade. The two-pass serpentine split passage has an aspect ratio of 14:1, tabulated passages, and a tip turning vane, all with the inclusion of channel convergence from root to tip, as well as channel taper toward the trailing edge. Local heat transfer and wall static pressure measurements show variations due to flow separation, turning flow, locally lower convection speeds, and impingement effects.

A number of other experimental investigations address flow behavior (without heat transfer) in channels with rib turbulators. Of these, Bonhoff et al.[78] and Schabacker et al.[79] consider nonrotating channels, and Tse and Steuber[80] and Prabhu and Vedula[81] consider rotating channels. In one case, different velocity components are measured in a serpentine channel with 45-deg ribs,[80] and in another, surface static pressure variations are measured with different channel aspect ratios and different rotational speeds in a rectangular channel with tranverse ribs on one wall.[81]

Computational studies of flows and heat transfer in ducts with rib turbulators consider straight single-pass ducts,[82–88] two-pass ducts,[89] two-pass ducts with U-shaped channels in between,[90–94] 90-deg orthogonal ribs,[82,84–87,93] 45-deg angled ribs,[83,88–92,94] 45-deg V-shaped ribs,[86] and rotation.[82,85,88–94] In one case,[83] the angled ribs placed on two opposite walls of the channel are rounded. The results from the most notable of these investigations with rotation show that the secondary flows induced by angled ribs, rotating buoyancy, and Coriolis forces produce important alterations to surface heat transfer coefficients and to local and global flowfield structure. This includes the development of strong nonisotropic turbulence stresses.[91,92] Jia et al.[86] and Watanabe and Takahashi[87] include experimentally measured friction factors, Nusselt numbers, and streamwise velocity fluctuations, which are compared to numerically predicted results. Rigby and Bunker[95] employ a full three-dimensional Navier–Stokes equation solver to investigate the same complex trailing-edge passage of a high-pressure turbine blade investigated experimentally by Bunker et al.[77]

Flow Structure in Channels with Rib Turbulators

Figure 21 presents schematic diagrams of flow patterns in ducts with rib turbulators from Cho et al.[61] According to these authors, remarkable enhancements of local and spatially averaged surface heat transfer rates are possible with rib turbulators, in spite of lowered local Nusselt numbers at certain locations along ribbed surfaces. In Fig. 21a, flow recirculation patterns around a single rib are shown. The largest of these zones is positioned just downstream of each rib and covers a considerable portion of the ribbed wall. Each of these recirculation zones is often considered to be a potential hot spot because it is associated with locally lower surface Nusselt numbers (see Ref. 58). The resulting nonuniform surface heat transfer variations can also result in additional concerns because of the development of significant thermal stresses. Such effects are more pronounced with angled ribs because lateral gradients in the surface heat transfer are present that are generally greater than for normal or 90-deg ribs. Downstream of the flow recirculation zone, downstream of each rib, is a line across the surface where streamlines reattach. Figure 21b shows the weak secondary flows that often form downstream of this reattachment line for 90-deg rib turbulators.[61] These are induced by nonuniform duct geometry as the flow develops in the streamwise direction.

With angled ribs, additional secondary flows are induced by flow skewing. Figure 21c presents schematic diagrams of the strong secondary flows induced by this effect for rib turbulators oriented at angles from 30 to 60 deg (Ref. 61). For ribs that are parallel to each other on opposite sides of the channel, a pair of counter-rotating flow cells are present. For ribs that are oriented perpendicular to each other on opposite channel walls, one cell of rotating flow is present. Consequently, the strong secondary flows produced by the parallel arrangement not only have stronger effects on surface heat transfer distributions but also produce greater pressure drops. Changes to the overall nature of these secondary flows are produced by changes to the relative streamwise locations of the rib arrays on opposite channel walls, that is, whether the rib arrays on the opposite walls are in line or staggered with respect to one another.[61]

Additional data about the effects of the cross-rib arrangement on flow structure are presented in Fig. 22. Here, flow structure measurements are given for the 45-deg rib arrangement shown in Fig. 22a. In Fig. 22b, an instantaneous flow visualization image shows weak secondary flows that are generally consistent with the weak secondary flows shown in Fig. 21b. The Fig. 21b image is illuminated in a spanwise-normal plane just downstream of the rib turbulator test section for $Re_H = 430$. These data are obtained at this low Reynolds number because diffusion and increased unsteadiness at higher Reynolds numbers result in smeared and unrecognizable flow patterns. The image in Fig. 22a extends in the vertical direction from the bottom to the top of the channel and in the horizontal direction over a distance of about 2.0 channel heights. The spanwise center of each image is then located at the spanwise center of the test section at $Z/D_h = 0.0$. The most important features in the image are two large vortex pairs (indicated by mushroom-shaped smoke patterns) that emanate from the bottom and top channel surfaces. These vortex pairs are formed by the effects of the ribs as they force air to and from both of these test surfaces. The vortices and the accompanying secondary flows aid convective processes for heat transfer augmentation by 1) increasing secondary advection of fluid between the central parts of the channel and regions near the wall and 2) producing regions with high, three-dimensional shear and high magnitudes of turbulence production over much of the channel cross section, thereby substantially increasing turbulence transport levels in all three coordinate directions.

Figures 22c and 22d presents time-averaged surveys of local streamwise velocity and local total pressure, measured in a spanwise-normal plane located just downstream of the rib turbulator test section (shown in Fig. 22a) for $Re_H = 8 \times 10^3$. The surveys extend about one channel height in each direction. The total pressure survey, given in Fig. 22d, is valuable because it provides information on the losses produced by the ribs. Note that deficits of streamwise velocity and total pressure are evident in the lower-left and upper-right regions of Figs. 22c and 22d. These are due to downstream parts of ribs located just upstream. Evidence of significant mixing and unsteadiness is also provided by the high degree of spanwise-uniformity of each quantity shown. This uniformity results because time averaging "smears" flow structural characteristics (produced by strong secondary flows) as they change position substantially with time.

Figure 23 presents secondary flow vectors numerically predicted in a channel with 90-deg rib turbulators from Jia et al.[86] for a Reynolds number based on channel hydraulic diameter of 3×10^4. The duct employed has a square cross section with ribs on one wall. The rib pitch to rib height ratio is 9, and the ratio of rib height to channel hydraulic diameter is 0.1. Figures 23a–23c show the vector distributions in two different spanwise-normal planes, where one is between two ribs (plane 1) and one is above a rib (plane 2). Each of these planes extends from a smooth side wall to a symmetry plane, thus covers one-half of a flow cross-sectional plane. In both cases, a large rotating flow cell is present in each half-cross-sectional plane of the one-sided ribbed duct.[86] For the views shown, the cells are rotating in the counterclockwise direction. Jia et al.[86] indicate that these secondary motions cause the maximum streamwise velocity to be present not at the spanwise symmetry plane, but "somewhere closer to the side walls." This is due to advection of fluid with higher streamwise momentum to regions closer to the side walls. Such secondary flow advection is part of an inflow region that is present near the corner of the ribbed wall and the smooth side wall. After leaving this inflow region, Figs. 23a–23c show that the fluid advects upward along the smooth side walls and then turns toward the spanwise symmetry plane.

Measured and predicted results from Watanabe and Takahashi[87] are shown in Fig. 24 for a channel with 90-deg rib turbulators with a Reynolds number based on channel hydraulic diameter

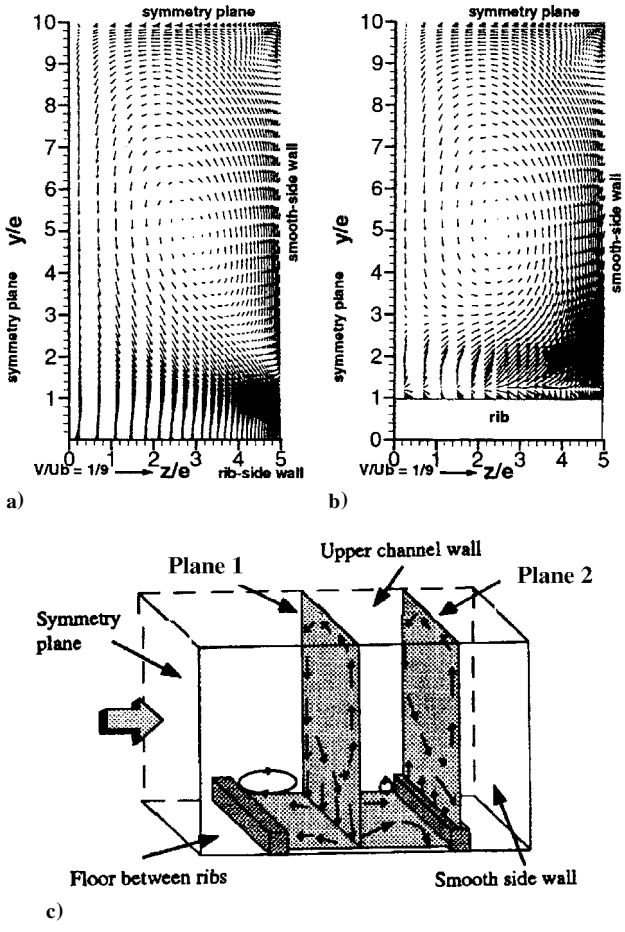

Fig. 23 Secondary flow vectors numerically predicted in a channel with 90-deg rib turbulators, from Jia et al.[86] for $Re_{Dh} = 3 \times 10^4$: a) secondary flow vectors in plane 1, b) secondary flow vectors in plane 2, and c) secondary flow structure conjectured from the numerical predictions.

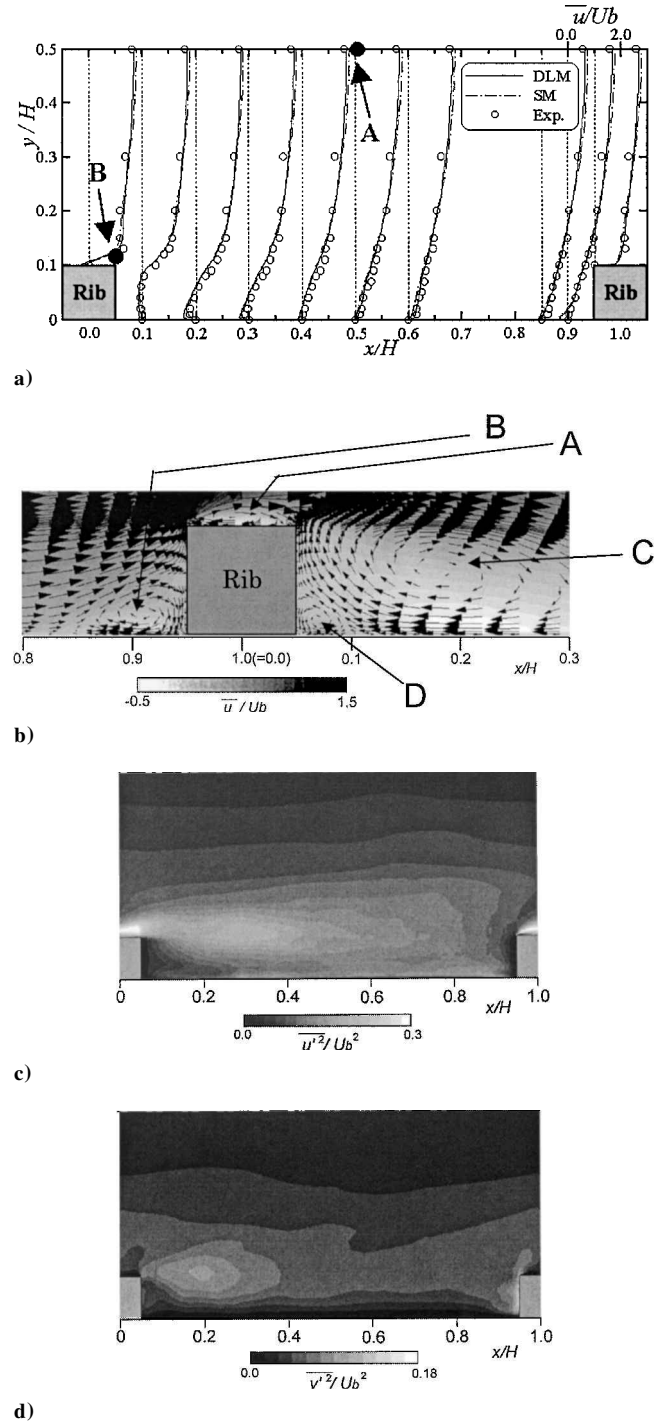

Fig. 24 Results for a channel with 90-deg rib turbulators, from Watanabe and Takahashi[87] for $Re_{Dh} = 1.17 \times 10^5$: a) time-averaged streamwise velocity variations above and between successive ribs from LES numerical simulations and experimental measurements, b) normalized streamwise velocity distribution and velocity vector distribution around a single rib from LES numerical simulations, c) normalized, time-averaged longitudinal velocity fluctuations above and between successive ribs from LES numerical simulations, and d) normalized, time-averaged normal velocity fluctuations above and between successive ribs from LES numerical simulations.

of 1.17×10^5. Figure 24a gives time-averaged streamwise velocity variations above and between successive ribs from large-eddy simulation (LES) numerical simulations and experimental measurements. The horizontal and vertical axes indicate the flow direction position and the distance along the test surface, respectively. Figure 24b shows the normalized streamwise velocity distribution and velocity vector distribution around a single rib from LES numerical simulations. These data are also time averaged. Features shown in Fig. 24b include the recirculation zone which forms just above the rib (denoted A) the recirculation zone that forms near the corner just upstream of the rib (denoted B) the large recirculation zone that is present downstream of the rib (denoted C), and the spanwise vortex, or second smaller separation zone, that is present in the vicinity of the downstream bottom corner of the rib (denoted D).

The same features are evident in experimental results presented in Fig. 25a from Casarsa et al.[57] These data are obtained in a channel with 90-deg rib turbulators at a Reynolds number based on channel hydraulic diameter of 4.0×10^4. Time-averaged distributions of flow streamlines are presented in Fig. 25a, as well as $(\bar{u}^2 + \bar{v}^2)^{1/2}$, the combined magnitude of time-averaged streamwise and normal velocity components. Because of the strong acceleration of flow as it passes around the rib, high-velocity gradients are present near the upstream top corner of the rib. The sudden expansion downstream of the rib results in the large recirculation zone C. A shear layer forms between this recirculating flow and the high-speed mainstream bulk flow, located just above.[57,87]

Figures 24c and 24d show distributions of normalized, time-averaged longitudinal velocity fluctuations and normal velocity fluctuations, respectively, above and between successive ribs from LES numerical simulations.[87] In each case, values are largest about one rib height away from the base wall, where the shear layer produced by the rib is strongest. After this shear layer reattaches, a new boundary layer develops, which is then accelerated by the mainstream flow as it approaches the next rib located downstream. The vorticity inside of this boundary layer gives origin to recirculation zone B, which forms in the corner just upstream of the next downstream rib.[57,87]

According to Casarsa et al.,[57] the shear layer reattachment line exhibits a particular shape near the lateral wall because side wall boundary layers are altered by the presence of the rib. When the

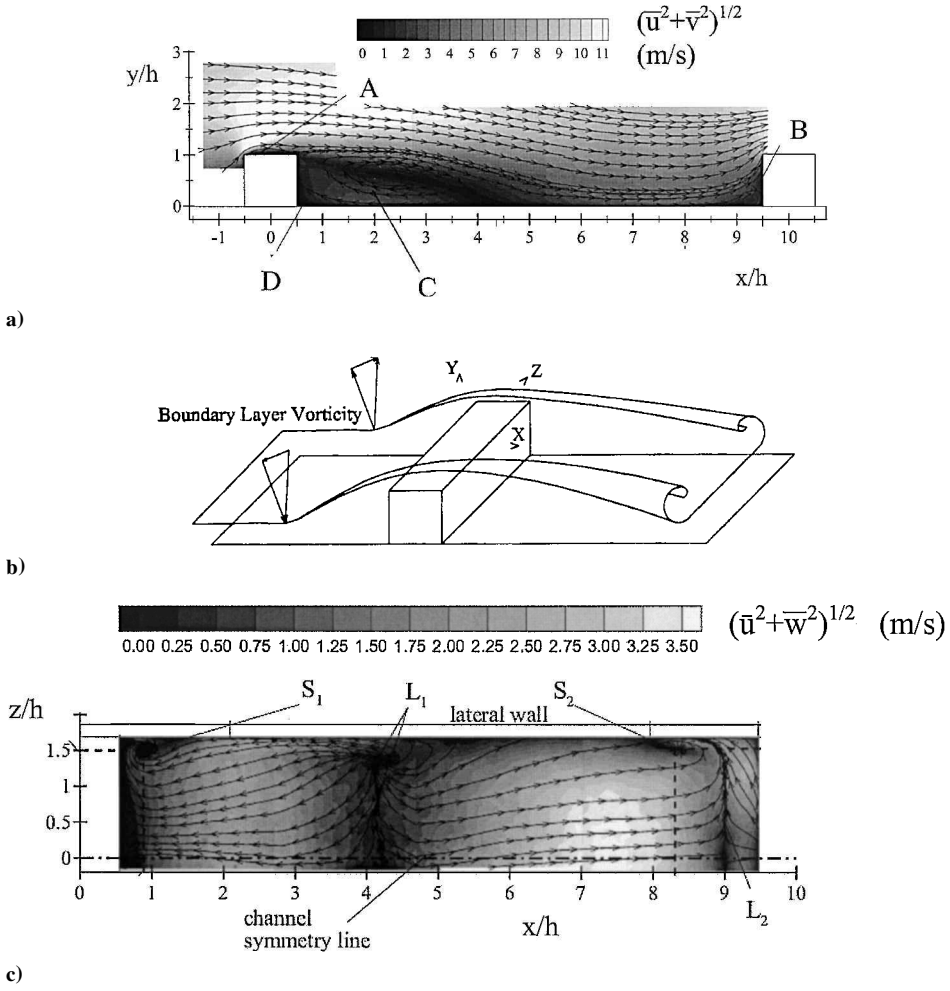

Fig. 25 Experimental results obtained in a channel with 90-deg rib turbulators, from Casarsa et al.[57] for $Re_{Dh} = 4.0 \times 10^4$: a) time-averaged velocity field measured in a streamwise-normal plane, b) schematic diagram of flow structure near the side walls of a ribbed passage, and c) time-averaged velocity field measured in a streamwise-spanwise plane.

boundary layer is deviated by the rib, new streamwise vorticity is generated inside of it. The flow then rolls up on itself,[57] as shown by the schematic diagram in Fig. 25b, which is based on experimental results shown in Fig. 25c. The result is local deformation of the reattachment line from a straight line. Presented in Fig. 25c are time-averaged flow streamlines, along with distributions of $(\bar{u}^2 + \bar{w}^2)^{1/2}$, measured in a spanwise-streamwise plane between adjacent ribs. Here, the reattachment line L_1 is apparent, including its deviation from a straight line near the lateral wall. Also apparent in front of the rib in Fig. 25c is the separation line L_2 associated with structure B. Notice that streamlines spiral around sink S_2. Similar behavior is also present just downstream of the rib near structure S_1. According to Casarsa et al.,[57] entrained mean flow generally moves toward the centerline in the vicinity of the reattachment line L_1 and toward the lateral wall in the vicinity of the rib.

Example of Spatially Resolved Surface Nusselt Number Distribution

Figure 26 presents a local surface Nusselt number ratio distribution from Ligrani and Mahmood[58] for $Re_H = 4.8 \times 10^4$ and $T_{0i}/T_w = 0.95$. These time-averaged results are measured over about two periods of ribbed pattern on the downstream portion the 45-deg rib turbulator test section shown in Fig. 22a. In Fig. 26, flow is directed from bottom to top in the increasing X/D_h direction.

The darker diagonal regions in Fig. 26 correspond to Nusselt number ratio Nu/Nu_0 values measured on the tops of the ribs. When compared along the rib tops, values are then highest near the upstream and downstream edges. This is partially due to flow recirculation zone A shown in Fig. 24b. As one moves from the rib in the streamwise or $+X/D_h$ direction, local Nusselt number ratio Nu/Nu_0 values initially decrease and then are low relative to other locations on the test surface. This is due to the spanwise vortex D

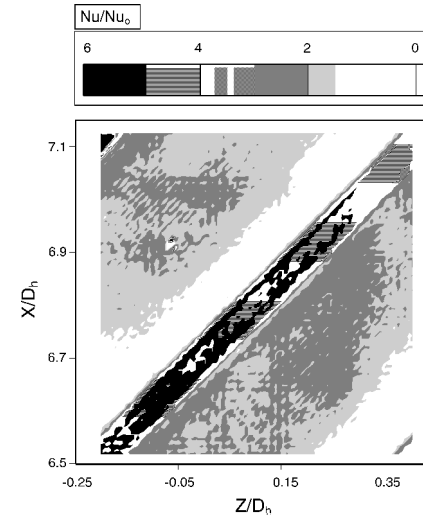

Fig. 26 Surface Nusselt number ratio distribution, from Mahmood et al.,[58] for downstream portion rib turbulator test section shown in Fig. 22a with 45-deg rib turbulators for $Re_H = 4.8 \times 10^4$.

and recirculating flow region C, both located just downstream of the rib, as shown in Fig. 24b. For the recirculation zone, flow direction next to the surface is opposite to the bulk flow direction. The region with relatively higher values of Nusselt number ratio Nu/Nu_0 then follows at slightly higher X/D_h (where $Nu/Nu_0 > 1.5$), which is due to reattachment of the shear layer that initially forms above the recirculation zone. With an additional increase in streamwise development, Nusselt number ratio Nu/Nu_0 values in Fig. 26 decrease

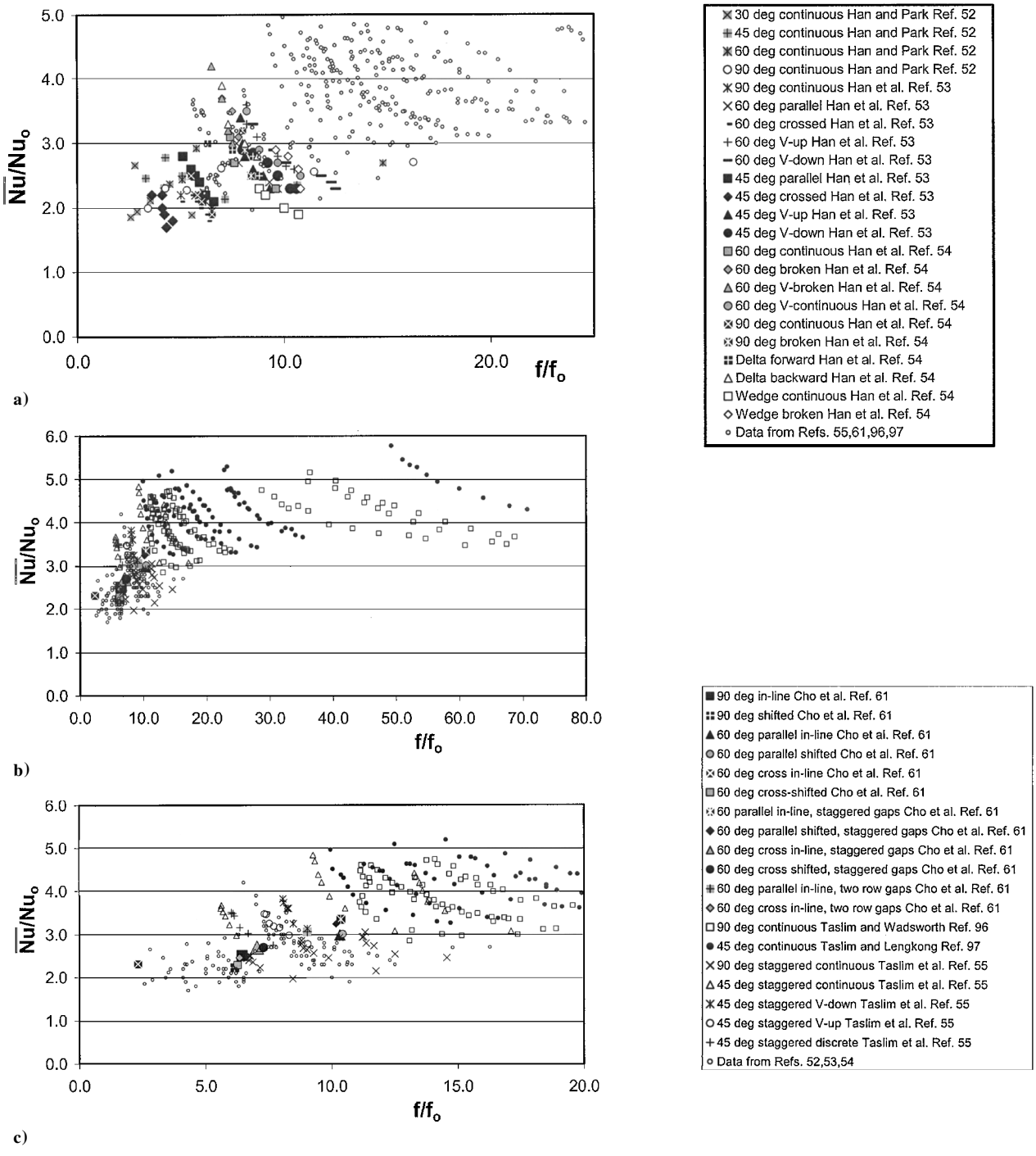

Fig. 27 Comparison of globally averaged Nusselt number ratios $\overline{Nu}/Nu_0$ as dependent on friction factor ratio f/f_0 from different rib turbulator investigations.[52–55,61,96,97] The same legend applies to parts b and c.

slightly once again (and then sometimes increase locally) as a second 45-deg rib is approached. These are due to the smaller region of recirculating flow (zone B) that forms just upstream of each rib turbulator, as shown in Fig. 24b. This pattern of flow and surface Nusselt number variations then repeats itself as additional ribs are encountered along the test surface. Other factors that affect the heat transfer augmenations are the skewing and three-dimensional nature of the boundary layer that develops due to the angled orientations of the ribs. Increased levels of three-dimensional turbulence production, turbulence transport, and the large-scale vortex pairs (shown in Fig. 22b) also make contributions.

Comparisons of Rib Turbulator Heat Transfer and Friction Factor Data

Figures 27a, 27b, and 27c compare rib turbulator data from different investigations[52–55,61,96,97] in Nusselt number ratio $\overline{Nu}/Nu_0$ vs friction factor ratio f/f_0 coordinates. Here, values range from 1.6 to 6.0 on the vertical scale and from 2 to 75 on the horizontal scale. The highest Nusselt number and friction factor augmentations are produced by the 45- and 90-deg continuous rib arrangements employed by Taslim and Wadsworth[96] and Taslim and Lengkong.[97] Note that the magnitudes of such augmentations often change significantly when a particular rib turbulator configuration is arranged with different rib height, different rib blockage, different rib pitch, or different relative spacing on opposite walls.

Swirl Chambers

Swirl chambers are internal flow passages arranged with either spinning vanes, internal inserts, or inlets and outlets configured to produce large-scale swirling of the flow (relative to the chamber dimensions) generally about the principal chamber axis.[98] This large-scale swirling and the Görtler vortex pairs that are formed enhance

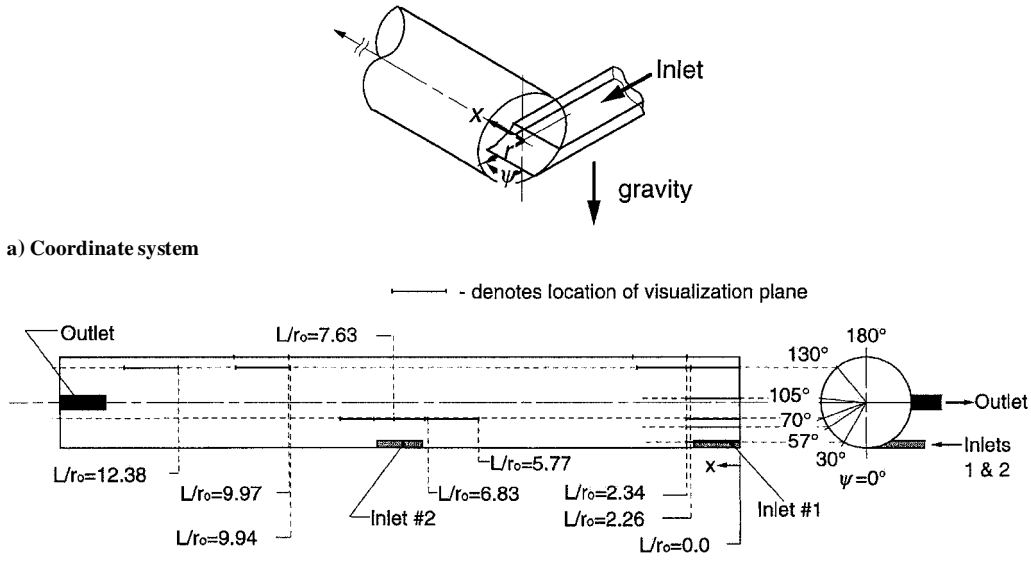

Fig. 28 Swirl chamber from Ligrani et al.[103] and Hedlund et al.[119,120]

surface heat transfer rates. Because of such unique flow and thermal characteristics, swirl chambers are applied to a considerable variety of engineering situations. They are used to fractionate solid particulates suspended and transported with liquids and gases, to enhance mixing processes in combustion chambers, to increase the quality at which critical heat flux occurs in two-phase flows, and for spray-drying applications when used with an atomizer. Devices producing large-scale swirling are also employed to enhance surface heat and mass transfer levels. As such, swirl chambers are employed in heat exchangers, automobile engines, furnaces, biomedical devices, and devices used for heating and cooling of metal ingots. Here, the heat transfer and fluid mechanics within swirl chambers are described as they are used to augment heat transfer rates for internal turbine blade cooling, an application recently introduced by Glezer et al.[99,100] A typical arrangement for this application is shown in Fig. 28.

Kreith and Margolis[101] first proposed that swirl induced in tube flows can augment surface heat transfer rates relative to unswirled flows. Khalatov and Zagumennov,[102] Glezer et al.,[99,100] Ligrani et al.,[103] Moon et al.[104] and others later employed tangential jets from wall slots to induce large-scale swirling in internal tube flows. Swirling flows are also induced in tubes using twisted tape inserts to augment measured surface heat transfer rates by a number of investigators, including Date[105] and Hong and Bergles.[106] Recent experimental investigations of fluid mechanics in swirl chambers with single-phase flow, wall injection, and no heat transfer include Kumar and Conover,[107] Dong and Lilley,[108] Bruun et al.,[109] Fitouri et al.,[110] and Chang and Dhir.[111] Rotating vanes, blades, propellers, or honeycombs are used near tube entrances by Sampers et al.,[112] Li and Tomita,[113] and Kok et al.[114] to induce swirl in adiabatic flows. Surveys of swirl flow investigations are presented by Gambil and Bundy,[115] Bergles,[116] Razgaitis and Holman,[117] and Papadopoulos et al.[118]

Hedlund et al.[119] and Hedlund and Ligrani[120] show that important variations of surface Nusselt numbers and time-averaged flow characteristics are present due to arrays of Goertler vortex pairs, especially near the inlets of the swirl chambers, where Nusselt numbers are highest. Nusselt numbers then decrease and become more spatially uniform along the interior surface of the chamber as the flows advect away from each inlet. Khalatov et al.[121] suggest the use of swirl chambers for heat transfer augmentation for friction factor ratios f/f_0 greater than 8.0–9.0 because fairly high heat transfer augmentation rates are obtained. However, simpler augmentation technologies are probably more advantageous at lower values of f/f_0, when overall thermal and hydraulic performance are considered together. The authors conclude that swirl chambers generally produce nonuniform heat transfer distributions in both the spanwise and circumferential directions. Hwang and Cheng[122] employ multiple swirling jets to augment heat transfer in a triangular duct. In some cases, the highest local heat transfer enhancements are produced on a bottom surface by wall jets, whereas in others, the highest local enhancements are produced on a target wall by impingement jets. Local and spatially averaged surface Nusselt numbers are given as they vary with Reynolds number and three different jet inlet angles.

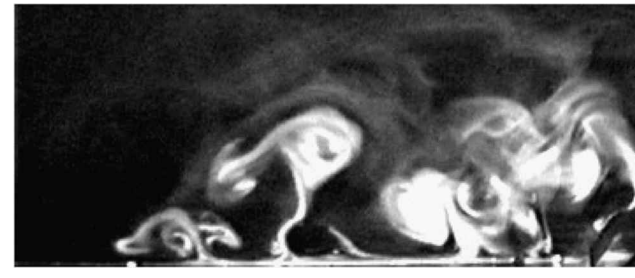

Fig. 29 Instantaneous flow image visualized in the axial/radial plane located at $\psi = 130$ deg and $L/r_0 = 9.94$ for $Re = 5.44 \times 10^3$; from Hedlund et al.[119]

Swirl Chamber Flow Structure

As mentioned, the configuration shown in Fig. 28 models an internal passage used to cool the leading edge of a turbine blade. Multiple inlets are employed at fixed locations to induce swirling,[103,119,120] which makes this swirl chamber geometry different from the arrangements used in many other investigations.

Figure 29 shows an instantaneous flow image visualized in the axial/radial plane located at $\psi = 130$ and $L/r_0 = 9.94$ for $Re = 5.44 \times 10^3$ (Ref. 119). This location is between the second inlet and the outlet shown in Fig. 28. The image in Fig. 29 shows convoluted Görtler vortex pairs in an instantaneous snapshot from a sequence of time-varying video images. Numerous Görtler vortex pairs of different size near the concave surface of the chamber are apparent, where each vortex pair is identified by a mushroom-shaped smoke pattern. The distortion of the mushroom-shaped smoke patterns evidences flow unsteadiness. Such vortex pairs increase in size, number, and distortion with streamwise development through the swirl chamber.[119] A new set of smaller Görtler vortex pairs then forms near the concave surface just downstream of the second swirl chamber inlet because of the growth of new shear layers near this location. As the flow continues to develop downstream, the vortex pairs not only become increasingly distorted because of flow unsteadiness, but also dramatically increase in size. Much of the skewness and three dimensionality of the Görtler vortex pairs, such as the ones shown in Fig. 29, are due to the axial component of flow in the swirl chamber. Also particularly apparent at these locations is the continuous interactions and intermingling of different-sized Görtler vortex pairs with each other. As the Reynolds number increases,

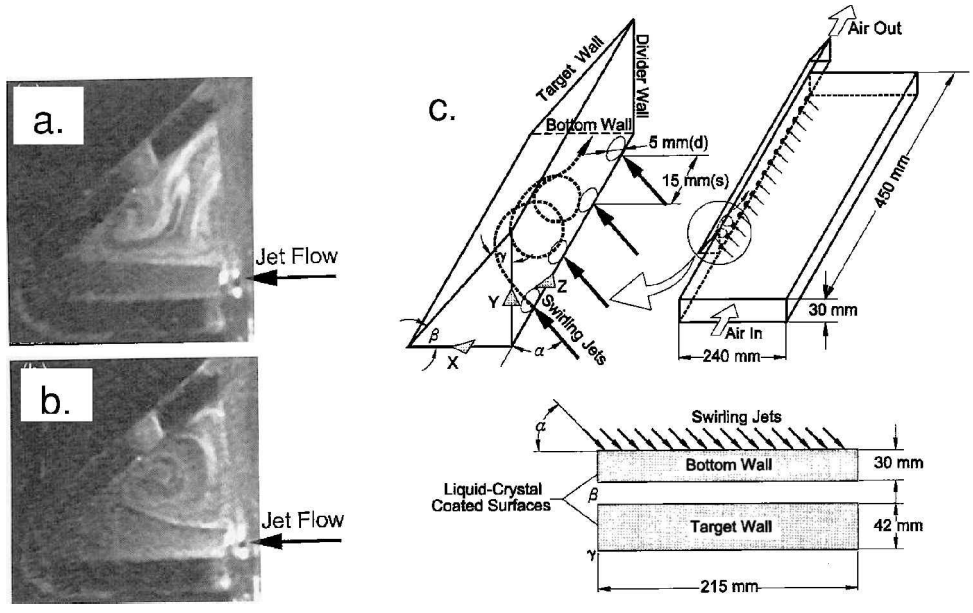

Fig. 30 Instantaneous flow visualization image, from Hwang and Cheng,[122] showing large-scale motions in a triangular shaped swirl chamber, at 4.5 injection hole diameters downstream of the inlet for inlet jet angles a) 75 deg and b) 45 deg with c) swirl chamber geometry.

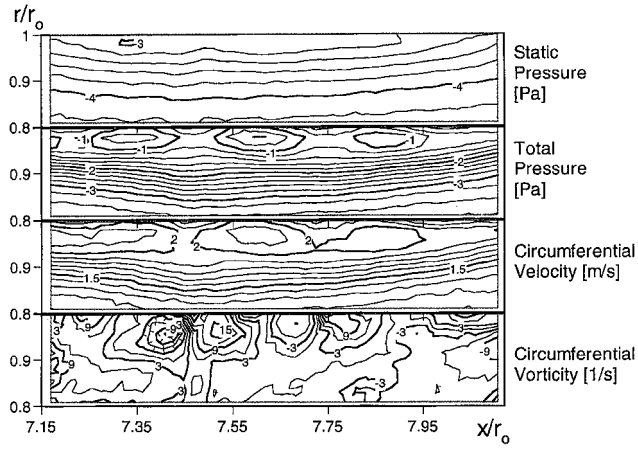

Fig. 31 Surveys of static pressure (relative to atmospheric inlet pressure), total pressure (relative to atmospheric inlet pressure), circumferential velocity, and circumferential vorticity at $\psi = 90$ deg and $Re = 1.8 \times 10^4$ for $L/r_0 = 7.15$–8.15 and $r/r_0 = 0.8$–1.0, from Hedlund et al.,[119] measured just downstream of second inlet of swirl chamber shown in Fig. 28.

interactions between adjacent vortex pairs generally become more intense, chaotic, and frequent.[103]

Figure 30 presents instantaneous flow visualization images, from Hwang and Cheng,[122] which show flow behavior in a triangular swirl chamber. The overall geometry of this chamber is shown in Fig. 30c. The images in Figs. 30a and 30b are obtained 4.5 injection hole diameters downstream of the inlet for two different inlet jet angles, 75 and 45 deg. This swirl chamber is a different arrangement than the one shown in Fig. 28 because none of the surfaces adjacent to the flow are concave. As a result, no Görtler vortex pairs develop. Instead, Fig. 30a shows that jet motions and large-scale motions are present in the triangular-shaped chamber. According to the authors, the jet produced by the 75-deg arrangement thoroughly washes the bottom wall and then directly impinges on the target plate. A counter-rotating vortex pair also forms around the upper portion of the duct. In Fig. 30b, the jets produced with the 45-deg angle lift off of the bottom wall turn into the mainstream and then produce a swirling motion in the center of the duct. This swirl in Fig. 30b appears to be larger and stronger than the double swirl motions shown in Fig. 30a. High surface heat transfer regions then develop where the swirling jets contact the surfaces of the chamber.

Figure 31 presents surveys of static pressure (relative to atmospheric inlet pressure), total pressure (relative to atmospheric inlet pressure), circumferential velocity, and circumferential vorticity for $Re = 1.8 \times 10^4$ from Hedlund et al.[119] These results are measured just downstream of the second inlet of the swirl chamber shown in Fig. 28. The measurement location is $\psi = 90$ deg, $r/r_0 = 0.8$–1.0, and $x/r_0 = 7.15$–8.15. Measurements at these locations provide data corresponding to initial Görtler vortex pair development. Distributions of circumferential vorticity in Fig. 31 show regions of positive and negative time-averaged circumferential vorticity adjacent to each other near the concave surface at $r/r_0 = 0.8$–1.0. Each of these evidences a pair of counter-rotating Görtler vortices that either are fairly steady or have preferred positions if they vary significantly in time. In Fig. 31, pairs of vorticity concentration of opposite sign are located at $x/r_0 = 7.3$–7.6 and $x/r_0 = 7.6$–7.9. Portions of pairs of vorticity concentration are evident in Fig. 31 at $x/r_0 < 7.3$ and $x/r_0 > 7.9$. Deficits of total pressure and circumferential velocity are present in upwash regions (where secondary flows are directed away from the concave surface), which are located between two regions of vorticity concentration of opposite sign in each vortex pair. These are located at or near x/r_0 of 7.2, 7.45, 7.75, and 8.0 in Fig. 31. Such results are important because they illustrate time-averaged Görtler vortex pair structure.

Figure 32 presents a composite schematic diagram of these flow features near the second inlet of a swirl chamber like the one shown in Fig. 28. Evident in Fig. 32 are large-scale motions from core swirling, secondary flows due to Görtler vortex pairs and shear layers that form on either side of the fluid that emerges from the inlet duct.

Example of Spatially Resolved Surface Nusselt Number Distribution

Figure 33 from Hedlund and Ligrani[120] presents a surface infrared image and a Nusselt number distribution that show surface variations due to Görtler vortex pairs for $Re = 1.215 \times 10^4$ and $T_{oi}/T_w = 0.86$ at $x/r_0 = 6.8$–8.2 and $\psi = 0$–80 deg. These are measured just downstream of the second inlet of the swirl chamber shown in Fig. 28. The infrared image in Fig. 33a shows surface variations due to Görtler vortex pairs in the form of light and dark stripes, which correspond to vortex pair trajectories along the concave surface of the chamber. Figure 33a is as recorded directly from an infrared camera with some enhancement but no corrections for camera angle and perspective. Surface temperature increases as image regions in Fig. 33a become lighter and whiter. Lower surface temperatures then coincide with higher local Nusselt numbers, and higher temperatures coincide with lower local Nusselt numbers.

Spatially resolved Nusselt numbers, determined from this infrared image, are shown in Fig. 33b. The oval shaped region at $x/r_0 = 7.1$–7.7 and $\psi = 0$–20 deg in Fig. 33b is located at the outlet of the second swirl chamber inlet duct. Important Nusselt number variations due

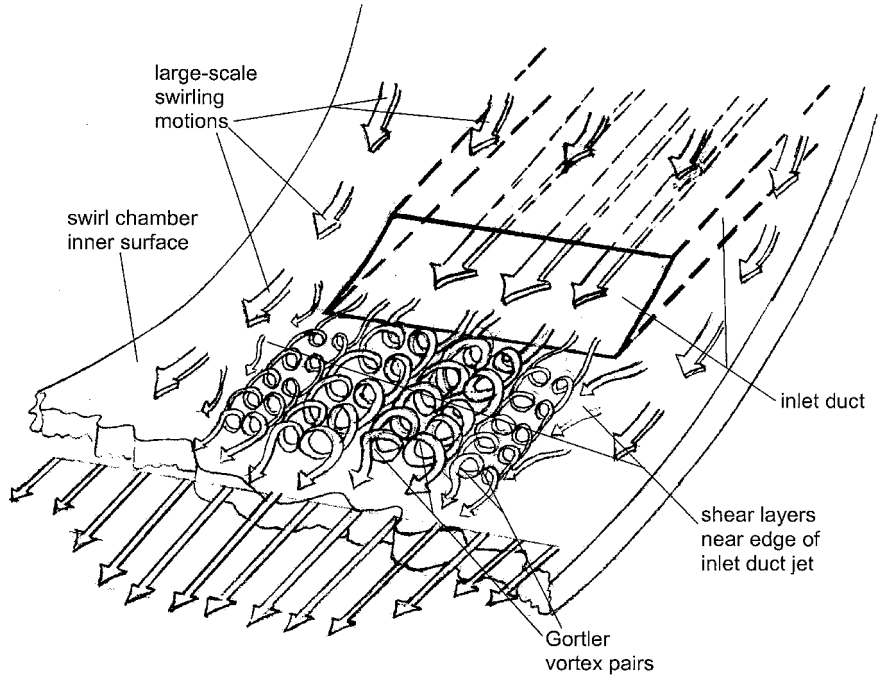

Fig. 32 Schematic diagram of the instantaneous, three-dimensional flow structure present near one swirl chamber inlet duct.

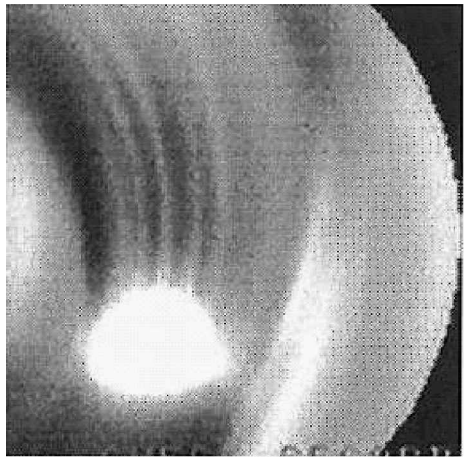

a) Enhanced infrared image

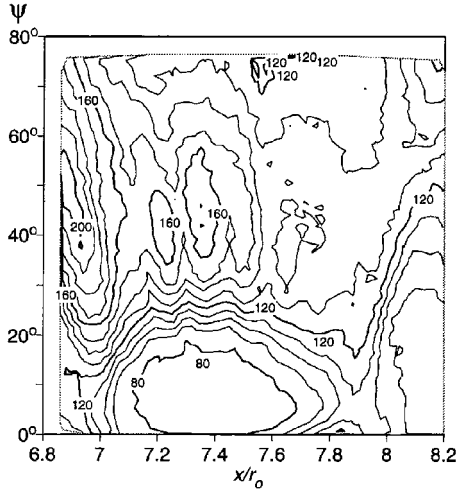

b) Nusselt number contours

Fig. 33 Surface Nusselt number distribution, which shows surface variations due to Görtler vortex pairs for $Re = 1.215 \times 10^4$ and $T_{0i}/T_w = 0.86$ at $x/r_0 = 6.8$–8.2 and $\psi = 0$–80 deg, from Hedlund and Ligrani,[120] measured just downstream of the second inlet of the swirl chamber shown in Fig. 28.

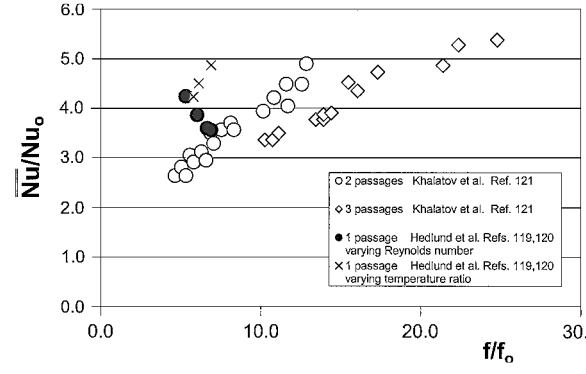

Fig. 34 Comparison of globally averaged Nusselt number ratios $\overline{Nu}/Nu_0$ as dependent on friction factor ratio f/f_0 from different swirl chamber investigations.[119–121]

to the Görtler vortex pairs are evident just above this location, where higher and lower local Nusselt numbers correspond to vortex pair downwash and upwash regions, respectively. Such variations are consistent with the contours of circumferential vorticity, circumferential velocity, total pressure, and static pressure shown in Fig. 31 for $\psi = 90$ deg. The high Nusselt number regions located at $x/r_0 = 6.8$–7.1 and at $x/r_0 = 8.0$–8.2 in Fig. 33b are due to the shear layers that form near the edges of the inlet jet. Because of these characteristics, Nusselt number gradients are present in both the axial and circumferential directions, and spatially resolved Nusselt number distributions, like the one shown in Fig. 33b, are highest near and just downstream of each swirl chamber inlet. As the flows advect away from each inlet, Nusselt numbers decrease and become more spatially uniform along the interior surface of the chamber.[119,120]

Local Nusselt numbers near each swirl chamber inlet are augmented by 1) centrifugal forces that force cool, high-density fluid near the hot surfaces by increasing amounts as T_{0i}/T_w decreases; 2) small-scale secondary flows within the arrays of initially developing Görtler vortex pairs; 3) continuous interactions and intermingling of different-sized Görtler vortex pairs with each other, especially at higher Reynolds numbers and at locations just downstream of inlet ducts (as shown in Fig. 29); 4) skewness and three dimensionality of Görtler vortex pairs produced by the axial component of flow in the swirl chamber; and 5) the shear layers that form on either sides of the jets that emerge from each inlet duct.[119,120]

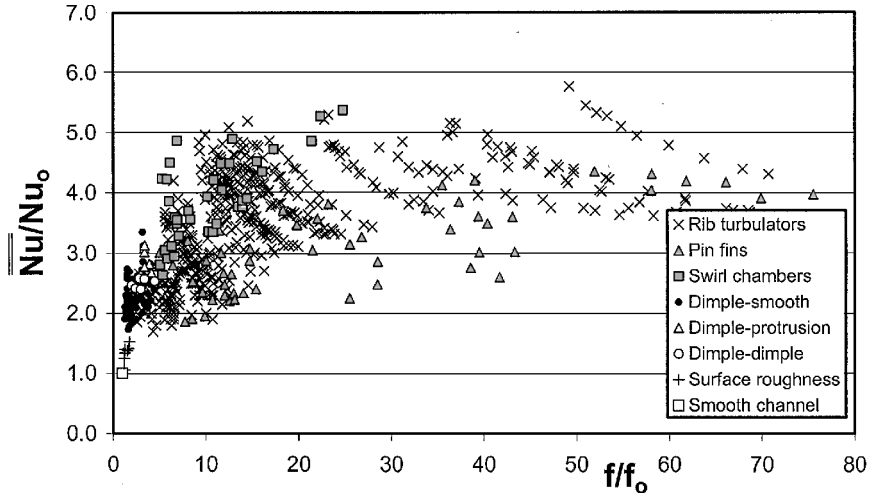

Fig. 35 Comparison of relative performance of rib turbulators, pin fins, swirl chambers, dimple–smooth arrangements, dimple–protrusion arrangements, dimple–dimple arrangements, surface roughness, and smooth-walled channels.

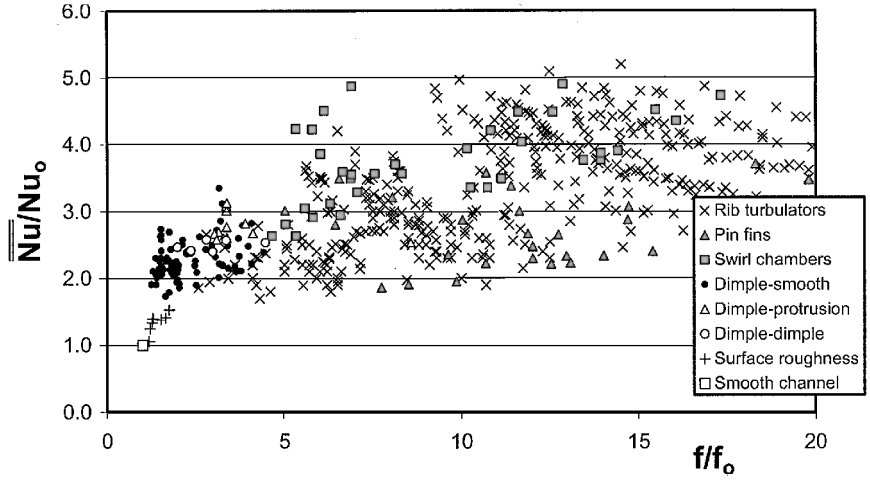

Fig. 36 Comparison of relative performance of rib turbulators, pin fins, swirl chambers, dimple–smooth arrangements, dimple–protrusion arrangements, dimple–dimple arrangements, surface roughness, and smooth-walled channels.

Comparisons of Swirl Chamber Heat Transfer and Friction Factor Data

Figure 34 compares swirl chamber data from different sources[119–121] in Nusselt number ratio $\overline{Nu}/Nu_0$ vs friction factor ratio f/f_0 coordinates. Here, values range from 2.5 to 5.5 on the vertical scale and from 4 to 26 on the horizontal scale. The experimental setup used by Khalatov et al.[121] consists of three passages numbered 1–3, where only passages 2 and 3 contain swirl flow. The experimental setup of Hedlund et al.[119,120] consists of only one passage. According to Fig. 34, the results from Hedlund et al.[119,120] for a single passage and the data from Khalatov et al.[121] for two passages yield lower friction factor ratios, whereas the data from Khalatov et al.[121] for three passages yield greater heat transfer augmentations.

Overall Comparisons

Figures 35 and 36 present comparisons of globally averaged Nusselt number ratios $\overline{Nu}/Nu_0$ and friction factor ratios f/f_0 for rib turbulators, pin fins, swirl chambers, dimple–smooth arrangements, dimple–protrusion arrangements, dimple–dimple arrangements, surface roughness, and smooth-walled channels. The f/f_0 abscissa scale in Fig. 36 ranges from 0 to 20 (compared to from 0 to 80 in Fig. 35) to provide a detailed view of variations over this friction factor ratio range.

Of the techniques considered, swirl chambers give some of the highest levels of heat transfer augmentation when compared at the same value of friction factor ratio. In some cases, several of the rib turbulator configurations produce comparable Nusselt number ratios. However, pressure losses and friction factor ratios associated with swirl chambers and rib turbulators are also relatively high. Many of the rib turbulator configurations produce levels of heat transfer augmentation that are higher than those produced by the dimple–protrusion–smooth configurations. However, generally, the increases in pressure losses due to the rib turbulators are also larger than those associated with the dimple–protrusion–smooth configurations. There are f/f_0 magnitudes as high as 71 for channels with rib turbulators and as high as 25 for swirl chambers, whereas magnitudes for dimple–protrusion–smooth configurations reach only up to 4.5. Nusselt number ratios in channels with pin fins lie near the bottom of or below the values for rib turbulators when compared at the same f/f_0 value. Pin-fin friction factor ratios are then as high as 76.

Also included in Figs. 35 and 36 are Nusselt number ratios and friction factor ratios for a smooth channel and for a channel with three-dimensional, irregular surface roughness.[123,124] Such surface roughness augmenters work as microturbulators and microvortex generators. These act to increase mixing and levels of turbulence transport locally near surfaces. With this mechanism, $\overline{Nu}/Nu_0$ range from 1.06 to 1.53, and f/f_0 range from 1.18 to 1.75 in Figs. 35 and 36.

The data in Figs. 35 and 36 are presented again in Figs. 37 and 38. In Fig. 37, globally averaged thermal performance parameters $\overline{Nu}/Nu_0/(f/f_0)^{1/3}$ are given as dependent on the friction factor ratio f/f_0. The form of this performance parameter is suggested by Gee and Webb[125] to provide a heat transfer augmentation quantity

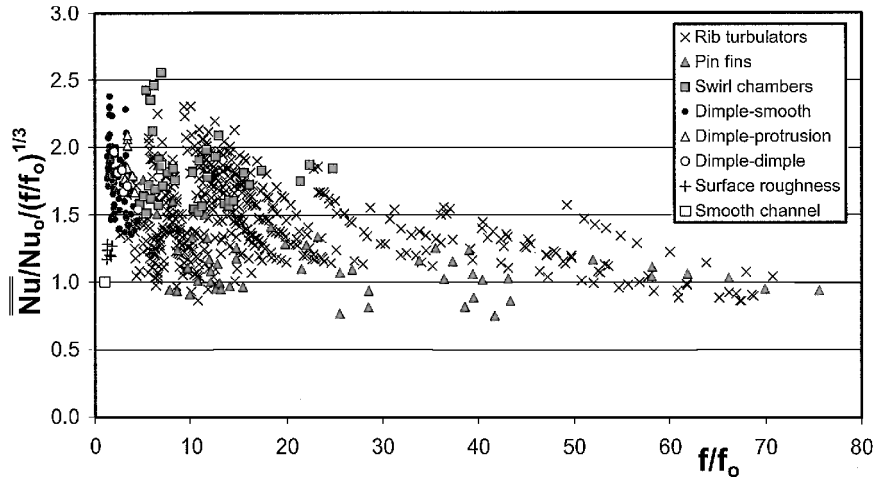

Fig. 37 Comparison of thermal performance parameters of rib turbulators, pin fins, swirl chambers, dimple–smooth arrangements, dimple–protrusion arrangements, dimple–dimple arrangements, surface roughness, and smooth-walled channels.

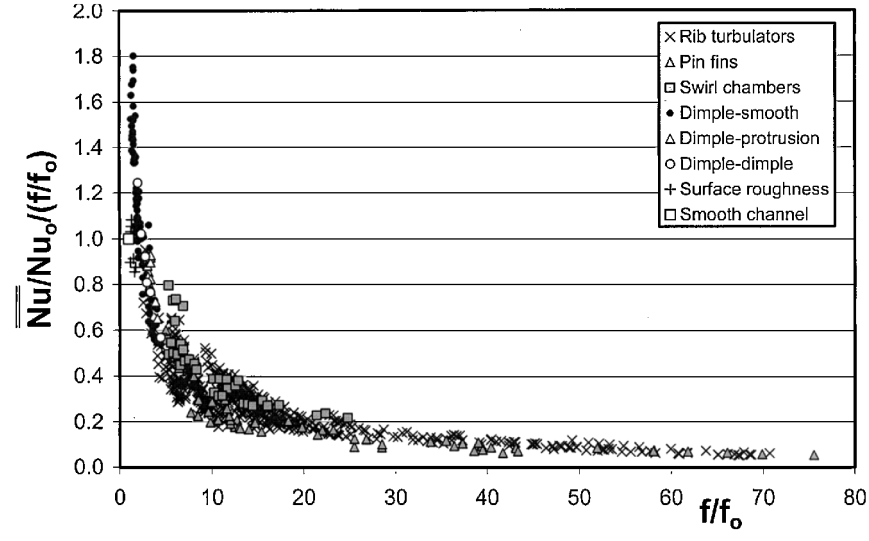

Fig. 38 Comparison of thermal performance parameters of rib turbulators, pin fins, swirl chambers, dimple–smooth arrangements, dimple–protrusion arrangements, dimple–dimple arrangements, surface roughness, and smooth-walled channels.

Nusselt number ratio $\overline{Nu}/Nu_0$ and a friction factor augmentation quantity $(f/f_0)^{1/3}$, where each is given for the same ratio of mass flux in an internal passage with augmentation devices to mass flux in an internal passage with smooth surfaces. According to Fig. 37, the highest $\overline{Nu}/Nu_0/(f/f_0)^{1/3}$ thermal performance parameters are produced by swirl chambers and dimple–smooth arrangements, and the lowest are produced by channels with arrays of pin fins. Results for rib turbulators, dimple–protrusion arrangements, dimple–dimple arrangements, surface roughness, and smooth-walled channels then generally lie between these distributions.

The $\overline{Nu}/Nu_0/(f/f_0)$ parameter, presented in Fig. 38, is referred to as the Reynolds analogy performance parameter. The highest values of this parameter are produced by dimple–smooth arrangements, and the lowest are produced by pin fins. Results for rib turbulators, swirl chambers, dimple–protrusion arrangements, dimple–dimple arrangements, surface roughness, and smooth-walled channels then generally lie between these distributions.

Summary

A variety of flow characteristics and mechanisms are responsible for the heat transfer augmentations and friction factor augmentations produced by pin fins, dimpled surfaces, surfaces with protrusions, ribbed turbulators, swirl chambers, and surface roughness.

For example, vortical structures and highly vortical fluid are important in flows over and around every one of these devices. The vortices take a variety of forms, including primary and secondary horseshoe vortices around pin fins, Görtler vortices near swirl chamber surfaces, vortices formed by periodic fluid motion into and out of dimples, vortexlike flows that accompany flow recirculation zones near rib turbulators and pin fins, and the microvortices and vortical motions formed by three-dimensional, irregular surface roughness. In some cases, interactions between vortices with different sizes, which are initiated at different locations, have important effects, as in flows near swirl chamber surfaces and in flows near dimpled surfaces.

Highly three-dimensional, skewed boundary layers are also present near all of the augmentation devices. In some cases, such as for flows near rib turbulators and near swirl chamber surfaces, such skewing increases mixing and interactions of fluid packets over a wide range of length scales. Flow recirculation and shear layer reattachment also play important heat transfer augmentation roles in flows around rib turbulators, protrusions, and roughness elements, as well as in flows within dimple cavities. Wakes are important because of the large-scale mixing that often occurs as they develop downstream and because of the shear layers that form near their edges at the interface between high-speed flow away from the wake and the lower-speed flow within the wake. Such wakes are present downstream of rib turbulators, roughness elements, and protrusions but are especially important for arrays of pin fins because wakes from upstream pins increase mixing as they advect in the vicinity of pins located farther downstream. The stagnation lines along the upstream edges of pin fins also aid augmentations because of

the initiation of thermal boundary layers at this location. Thermal boundary-layer initiation and the high heat transfer rates that accompany the presence of extremely thin thermal boundary layers are also present near the exits of swirl chamber entrance ducts. Thermal boundary layers are also reinitialized in a periodic fashion, at locations just downstream of individual dimples.

These same phenomena are also responsible for the different friction factor ratios produced by the different devices. For example, friction factor ratios as high as 71–76 are a result of the wakes, recirculation flow zones, significant flow blockage, and form drag produced by pin fins and rib turbulators. As a result, the lowest thermal performance parameters are measured in flows through passages with pin fins and some types of rib turbulators. The high mixing produced by other rib arrangements are accompanied by relatively low friction factor ratios and result in $\overline{Nu}/Nu_0/(f/f_0)^{1/3}$ performance parameters as high as 2.3 and $\overline{Nu}/Nu_0/(f/f_0)$ performance parameters as high as 1.1. Relatively low friction factor ratios are also present in flows over dimpled surfaces because they do not protrude into the flow and, therefore, produce almost no form drag. Resulting friction factor ratios are only as high as 4.5, with $\overline{Nu}/Nu_0/(f/f_0)^{1/3}$ performance parameters up to 2.4 and $\overline{Nu}/Nu_0/(f/f_0)$ performance parameters up to 1.8. The relatively high thermal performance parameters produced by swirl chambers are a result of friction factor ratios as high as 25 and mixing that occurs over a broad range of length scales.

From a practical perspective, the overall objective of each device examined, and future heat augmentation devices under development, is high-thermal-performance parameters. This is accomplished by increasing surface areas for convective heat transfer and by enhancing convective heat transfer coefficients, with minimal increases in streamwise pressure drop penalties and skin-friction coefficients. When the thermal and Reynolds stress transport equations are considered, heat transfer coefficients are generally augmented by two mechanisms: 1) increasing secondary advection of heat away from surfaces and 2) increasing magnitudes of three-dimensional turbulence transport and three-dimensional turbulence production by increasing shear and creating larger gradients of velocity. All of the devices discussed accomplish these two tasks in one way or another. In some cases, this is done by augmenting secondary flows and turbulence levels to enhance mixing and in others by forming coherent fluid motions in the form of streamwise oriented vortices and/or vortex pairs. Improvements can be made by accomplishing such tasks not only at specific locations and zones in each flow, but over larger volumetric portions of the different flowfields.

Acknowledgments

This paper was prepared under the sponsorship of Pratt and Whitney—Canada Corp. Many individuals contributed experimental results, numerical results, publication copies, or valuable discussions that aided in the preparation of this paper, including T. Arts, R. Bunker, C. Camci, H. H. Cho, M.-K. Chyu, D. Kercher, S. Lau, T. I-P. Shih, and K. Watanabe. Some of the results contained within this paper are based on measurements conducted at the University of Utah by many individuals, including H. H. Jung, S. W. Lee, and a number of graduate and undergraduate students, T. R. Babinchak, N. K. Burgess, E. Comeau, J. Hanson, C. R. Hedlund, D. Kenney, G. I. Mahmood, S. Peddicord, R. Thambu, and S. Y. Won.

References

[1]Han, J. C., Park, J. S., and Lie, C. K., "Heat Transfer and Pressure Drop in Blade Cooling Channels with Turbulence Promoters," NASA CR-3837, 1984.

[2]Han, J. C., Dutta, S., and Ekkad, S., *Gas Turbine Heat Transfer and Cooling Technology*, Taylor and Francis, New York, 2000, pp. 6, 7, 251–254.

[3]Lau, S. C., "Enhanced Internal Cooling of Gas Turbine Airfoils," *Heat Transfer in Gas Turbines*, edited by S. Sunden, and M. Faghri, WIT Press, Southampton, England, U.K., 2001, pp. 109–175.

[4]Brigham, A. W., and Van Fossen, G. J., "Length to Diameter Ratio and Row Number Effects in Short Pin Fin Heat Transfer," *Journal of Engineering for Gas Turbines and Power*, Vol. 106, No. 1, 1984, pp. 241–245.

[5]Ligrani, P. M., and Mahmood, G. I., "Variable Property Nusselt Numbers in a Channel with Pin Fins," *Journal of Thermophysics and Heat Transfer*, Vol. 17, No. 1, 2003, pp. 103–111.

[6]Zukauskas, A., "Heat Transfer from Tubes in Cross Flow," *Advances in Heat Transfer*, Vol. 8, 1972, pp. 96–160.

[7]Sparrow, E. M., Ramsey, J. W., and Altemani, C. A. C., "Experiments on In-Line Pin Fin Arrays and Performance Comparisons with Staggered Array," *Journal of Heat Transfer*, Vol. 102, No. 1, 1980, pp. 44–50.

[8]Metzger, D. E., and Haley, S. W., "Heat Transfer Experiments and Flow Visualization for Arrays of Short Pin-Fins," American Society of Mechanical Engineers, International Gas Turbine and Aeroengine Congress and Exhibition, ASME Paper 82-GT-138, June 1982.

[9]Metzger, D. E., Barry, R. A., and Bronson, J. P., "Developing Heat Transfer in Rectangular Ducts with Staggered Arrays of Short Pin-Fins," *Journal of Heat Transfer*, Vol. 104, No. 4, 1982, pp. 700–706.

[10]Van Fossen, G. J., "Heat-Transfer Coefficients For Staggered Arrays of Short Pin-Fins," *Journal of Engineering for Power*, Vol. 104, No. 2, 1982, pp. 268–274.

[11]Simoneau, R. J., and Van Fossen, G. J., "Effects of Location in an Array on Heat Transfer to a Short Cylinder in Cross Flow," *Journal of Heat Transfer*, Vol. 106, No. 1, 1984, pp. 42–48.

[12]Lau, S. C., Han, J. C., and Kim, Y. S., "Turbulent Heat Transfer and Friction in Pin Fin Channels with Lateral Flow Ejection," *Journal of Heat Transfer*, Vol. 111, No. 1, 1989, pp. 51–58.

[13]McMillin, R. D., and Lau, S. C., "Effects of Trailing-Edge Ejection on Local Heat (Mass) Transfer in Pin Fin Cooling Channels in Turbine Blades," *Journal of Turbomachinery*, Vol. 116, No. 1, 1994, pp. 159–168.

[14]Chyu, M. K., "Heat Transfer and Pressure Drop for Short Pin-Fin Arrays with Pin-Endwall Fillet," *Journal of Heat Transfer*, Vol. 112, No. 4, 1990, pp. 926–932.

[15]Chyu, M. K., and Goldstein, R. J., "Influence of an Array of Wall-Mounted Cylinders on the Mass Transfer from a Flat Surface," *International Journal of Heat and Mass Transfer*, Vol. 34, No. 9, 1991, pp. 2175–2186.

[16]Chyu, M. K., Hsing, Y. C., Shih, T. I.-P., and Natarajan, V., "Heat Transfer Contributions of Pins and Endwall in Pin-Fin Arrays: Effects of Thermal Boundary Condition Modeling," *Journal of Turbomachinery*, Vol. 121, No. 2, 1999, pp. 257–263.

[17]Grannis, V. B., and Sparrow, E. M., "Numerical Simulation of Fluid Flow Through an Array of Diamond Shaped Pin Fins," *Numerical Heat Transfer*, Pt. A, Vol. 19, 1991, pp. 381–403.

[18]Olson, D. A., "Heat Transfer in Thin, Compact Heat Exchangers with Circular, Rectangular, or Pin-Fin Flow Passages," *Journal of Heat Transfer*, Vol. 114, No. 2, 1992, pp. 373–382.

[19]Chyu, M. K., and Natarajan, V., "Heat Transfer on the Base Surface of Three-Dimensional Protruding Elements," *International Journal of Heat and Mass Transfer*, Vol. 39, No. 14, 1996, pp. 2925–2935.

[20]Chyu, M. K., Hsing, Y. C., and Natarajan, V., "Convective Heat Transfer of Cubic Fin Arrays in a Narrow Channel," *Journal of Turbomachinery*, Vol. 120, No. 2, 1998, pp. 362–367.

[21]Hwang, J. J., and Lu, C. C., "Lateral-Flow Effect on Endwall Heat Transfer and Pressure Drop in a Pin-Fin Trapezoidal Duct of Various Pin Shapes," American Society of Mechanical Engineers, 45th International Gas Turbine and Aeroengine Congress and Exhibition, Munich, ASME Paper 2000-GT-232, May 2000.

[22]Uzol, O., and Camci, C., "Elliptical Pin Fins as an Alternative to Circular Pin Fins for Gas Turbine Blade Cooling Applications. Part 1: Endwall Heat Transfer and Total Pressure Loss Characteristics," American Society of Mechanical Engineers, 46th International Gas Turbine and Aeroengine Congress and Exhibition, New Orleans, LA, ASME Paper 2001-GT-180, June 2001.

[23]Uzol, O., and Camci, C., "Elliptical Pin Fins as an Alternative to Circular Pin Fins for Gas Turbine Blade Cooling Applications. Part 2: Wake Flow Field Measurements and Visualization Using Particle Image Velocimetry," American Society of Mechanical Engineers, 46th International Gas Turbine and Aeroengine Congress and Exhibition, New Orleans, LA, ASME Paper 2001-GT-181, June 2001.

[24]Mahmood, G. I., Won, S. Y., and Ligrani, P. M., "Local Nusselt Numbers and Flow Structure in a Rectangular Channel with Cylindrical Pin-Fins," Dept. of Mechanical Engineering, Univ. of Utah, Salt Lake City, UT, Dec. 2002.

[25]Al Dabagh, A. M., and Andrews, G. E., "Pin-Fin Heat Transfer: Contribution of the Wall and the Pin to the Overall Heat Transfer," American Society of Mechanical Engineers, ASME Paper 92-GT-242, 1992.

[26]Murzin, V. N., Stoklitskii, S. A., and Chebotarev, A. P., "Creation of Solitary Vortices in a Flow Around Shallow Spherical Depressions," *Soviet Technical Physical Letters*, Vol. 12, No. 11, 1986, pp. 547–549.

[27]Gromov, P. R., Zobnin, A. B., Rabinovich, M. I., and Sushchik, M. M., "Creation of Solitary Vortices in a Flow Around Shallow Spherical Depressions," *Soviet Technical Physical Letters*, Vol. 12, No. 11, 1986, pp. 1323–1328.

[28]Kesarev, V. S., and Kozlov, A. P., "Convective Heat Transfer in Turbulized Flow past a Hemispherical Cavity," *Heat Transfer Research*, Vol. 25, No. 2, 1993, pp. 156–160.

[29]Afanasyev, V. N., Chudnovsky, Y. P., Leontiev, A. I., and Roganov, P. S., "Turbulent Flow Friction and Heat Transfer Characteristics for Spherical Cavities on a Flat Plate," *Experimental Thermal and Fluid Science*, Vol. 7, 1993, pp. 1–8.

[30]Belen'kiy, M. Y., Gotovskiy, M. A., Lekakh, B. M., Fokin, B. S., and Dolgushin, K. S., "Heat Transfer Augmentation Using Surfaces Formed by a System of Spherical Cavities," *Heat Transfer Research*, Vol. 25, No. 2, 1993, pp. 196–203.

[31]Terekhov, V. I., Kalinina, S. V., and Mshvidobadze, Y. M., "Flow Structure and Heat Transfer on a Surface with a Unit Hole Depression," *Russian Journal of Engineering Thermophysics*, Vol. 5, 1995, pp. 11–34.

[32]Zhak, V. D., "The Taylor–Goertler Vortices and Three-Dimensional Flow Evolution in a Cavity," *Russian Journal of Engineering Thermophysics*, Vol. 5, 1995, pp. 165–176.

[33]Schukin, A. V., Kozlov, A. P., and Agachev, R. S., "Study and Application of Hemispheric Cavities for Surface Heat Transfer Augmentation," American Society of Mechanical Engineers, 40th International Gas Turbine and Aeroengine Congress and Exhibition, Houston, TX, ASME Paper 95-GT-59, June 1995, pp. 1–6.

[34]Bearman, P. W., and Harvey, J. K., "Control of Circular Cylinder Flow by the Use of Dimples," *AIAA Journal*, Vol. 31, No. 10, 1993, pp. 1753–1756.

[35]Kimura, T., and Tsutahara, M., "Fluid Dynamic Effects of Grooves on Circular Cylinder Surfaces," *AIAA Journal*, Vol. 29, No. 12, 1991, pp. 2062–2068.

[36]Kithcart, M. E., and Klett, D. E., "Heat Transfer and Skin Friction Comparison of Dimpled Versus Protrusion Roughness," *Journal of Enhanced Heat Transfer*, Vol. 3, No. 4, 1996, pp. 273–280.

[37]Chyu, M. K., Yu, Y., Ding, H., Downs, J. P., and Soechting, F. O., "Concavity Enhanced Heat Transfer in an Internal Cooling Passage," American Society of Mechanical Engineers, 42nd International Gas Turbine and Aeroengine Congress and Exhibition, Orlando, FL, ASME Paper 97-GT-437, June 1997, pp. 1–7.

[38]Lin, Y. L., Shih, T. I-P., and Chyu, M. K., "Computations of Flow and Heat Transfer in a Channel with Rows of Hemispherical Cavities," American Society of Mechanical Engineers, 44th International Gas Turbine and Aeroengine Congress and Exhibition, Indianapolis, IN, ASME Paper 99-GT-263, June 1999, pp. 1–6.

[39]Gortyshov, Y. F., Popov, I. A., Amirkhanov, R. D., and Gulitsky, K. E., "Studies of Hydrodynamics and Heat Exchange in Channels with Various Types of Intensifiers," *Proceedings of the Eleventh International Heat Transfer Conference*, Kyongju, Republic of Korea, Vol. 6, 1998, pp. 83–88.

[40]Moon, H. K., O'Connell, T., and Glezer, B., "Channel Height Effect on Heat Transfer and Friction in a Dimpled Passage," American Society of Mechanical Engineers, 44th International Gas Turbine and Aeroengine Congress and Exhibition, Indianapolis, IN, ASME Paper 99-GT-163, June 1999, pp. 1–8.

[41]Syred, N., Khalatov, A., Kozlov, A., Shchukin, A., and Agachev, R., "Effect of Surface Curvature on Heat Transfer and Hydrodynamics within a Single Hemispherical Dimple," *Journal of Turbomachinery*, Vol. 123. No. 3, 2001, pp. 609–613.

[42]Chen, J., Muller-Steinhagen, H., and Duffy, G. G., "Heat Transfer Enhancement in Dimpled Tubes," *Applied Thermal Engineering*, Vol. 21, 2001, pp. 535–547.

[43]Mahmood, G. I., Hill, M. L., Nelson, D. L., Ligrani, P. M., Moon, H.-K., and Glezer, B., "Local Heat Transfer and Flow Structure on and Above a Dimpled Surface in a Channel," *Journal of Turbomachinery*, Vol. 123, No. 1, 2001, pp. 115–123.

[44]Mahmood, G. I., and Ligrani, P. M., "Heat Transfer in a Dimpled Channel: Combined Influences of Aspect Ratio, Temperature Ratio, Reynolds Number, and Flow Structure," *International Journal of Heat and Mass Transfer*, Vol. 45, No. 10, 2002, pp. 2011–2020.

[45]Ligrani, P. M., Harrison, J. L., Mahmood, G. I., and Hill, M. L., "Flow Structure due to Dimple Depression on a Channel Surface," *Physics of Fluids*, Vol. 13, No. 11, 2001, pp. 3442–3451.

[46]Mahmood, G. I., Sabbagh, M. Z., and Ligrani, P. M., "Heat Transfer in a Channel with Dimples and Protrusions on Opposite Walls," *Journal of Thermophysics and Heat Transfer*, Vol. 15, No. 3, 2001, pp. 275–283.

[47]Ligrani, P. M., Mahmood, G. I., Harrison, J. L., Clayton, C. M., and Nelson, D. L., "Flow Structure and Local Nusselt Number Variations in a Channel with Dimples and Protrusions on Opposite Walls," *International Journal of Heat and Mass Transfer*, Vol. 44, No. 23, 2001, pp. 4413–4425.

[48]Isaev, S. A., Leont'ev, A. I., and Baranov, P. A., "Identification of Self-Organized Vortexlike Structures in Numerically Simulated Turbulent Flow of a Viscous Incompressible Liquid Streaming Around a Well on a Plane," *Turbulent Physics Letters*, Vol. 26, No. 1, 2000, pp. 15–18.

[49]Burgess, N. K., Oliveira, M. M., and Ligrani, P. M., "Nusselt Number Behavior on Deep Dimpled Surfaces Within a Channel," American Society of Mechanical Engineers, International Mechanical Engineering Congress and Exhibition, New Orleans, LA, ASME Paper IMECE2002-32941, Nov. 2002, pp. 1–9.

[50]Moon, S. W., and Lau, S. C., "Turbulent Heat Transfer Measurements on a Wall with Concave and Cylindrical Dimples in a Square Channel," American Society of Mechanical Engineers, 47th International Gas Turbine and Aeroengine Congress and Exhibition, Amsterdam, ASME Paper GT-2002-30208, June 2002, pp. 1–9.

[51]Han, J. C., Glicksman, L. R., and Rohsenow, W. M., "An Investigation of Heat Transfer and Friction for Rib-Roughened Surfaces," *International Journal of Heat and Mass Transfer*, Vol. 21, No. 7, 1978, pp. 1143–1156.

[52]Han, J. C., and Park, J. S., "Developing Heat Transfer in Rectangular Channels with Rib Turbulators," *International Journal of Heat and Mass Transfer*, Vol. 31, No. 1, 1988, pp. 183–195.

[53]Han, J. C., Zhang, Y. M., and Lee, C. P., "Augmented Heat Transfer in Square Channels with Parallel, Crossed, and V-Shaped Angled Ribs," *Journal of Heat Transfer*, Vol. 113, No. 3, 1991, pp. 590–596.

[54]Han, J. C., Huang, J. J., and Lee, C. P., "Augmented Heat Transfer in Square Channels with Wedge-Shaped and Delta-Shaped Turbulence Promoters," *Enhanced Heat Transfer*, Vol. 1, No. 1, 1993, pp. 37–52.

[55]Taslim, M. E., Li, T., and Kercher, D. M., "Experimental Heat Transfer and Friction in Channels Roughened with Angled, V-Shaped, and Discrete Ribs on Two Opposite Walls," *Journal of Turbomachinery*, Vol. 118, No. 1, 1996, pp. 20–28.

[56]Taslim, M. E., Li, T., and Spring, S. D., "Measurements of Heat Transfer Coefficients and Friction Factors in Passages Rib-Roughened on All Walls," *Journal of Turbomachinery*, Vol. 120, No. 3, 1998, pp. 564–570.

[57]Casarsa, L., Cakan, M., and Arts, T., "Characterization of the Velocity and Heat Transfer Fields in an Internal Cooling Channel with High Blockage Ratio," American Society of Mechanical Engineers, 47th International Gas Turbine and Aeroengine Congress and Exhibition, Amsterdam, ASME Paper GT-2002-30207, June 2002, pp. 1–8.

[58]Ligrani, P. M., and Mahmood, G. I., "Spatially-Resolved Heat Transfer and Flow Structure in a Rectangular Channel with 45° Angled Rib Turbulators," *Journal of Turbomachinery* (to be published).

[59]Wang, Z., Ireland, P. T., Kohler, S. T., and Chew, J. W., "Heat Transfer Measurements to a Gas Turbine Cooling Passage with Inclined Ribs," *Journal of Turbomachinery*, Vol. 120, No. 1, 1998, pp. 63–69.

[60]Thurman, D., and Poinsatte, P., "Experimental Heat Transfer and Bulk Air Temperature Measurements for a Multipass Internal Cooling Model with Ribs and Bleed," American Society of Mechanical Engineers, 45th International Gas Turbine and Aeroengine Congress and Exhibition, Munich, ASME Paper 2000-GT-233, May 2000, pp. 1–13.

[61]Cho, H. H., Lee, S. Y., and Wu, S. J., "The Combined Effects of Rib Arrangements and Discrete Ribs on Local Heat/Mass Transfer in a Square Duct," American Society of Mechanical Engineers, 46th International Gas Turbine and Aeroengine Congress and Exhibition, New Orleans, LA, ASME Paper 2001-GT-175, June 2001, pp. 1–11.

[62]Johnson, B. V., Wagner, J. H., Steuber, G. D., and Yeh, F. C., "Heat Transfer in Rotating Serpentine Passage with Trips Skewed to the Flow," *Journal of Turbomachinery*, Vol. 116, No. 1, 1994, pp. 113–123.

[63]Fann, S., Yang, W. J., and Zhang, N., "Local Heat Transfer in a Rotating Serpentine Passage with Rib-Roughened Surfaces," *International Journal of Heat and Mass Transfer*, Vol. 37, No. 2, 1994, pp. 217–228.

[64]Parsons, J. A., Han, J. C., and Zhang, Y. M., "Wall Heating Effect on Local Heat Transfer in a Rotating Two-Pass Square Channel with Rib Turbulators," *International Journal of Heat and Mass Transfer*, Vol. 37, No. 9, 1994, pp. 1411–1420.

[65]Johnson, B. V., Wagner, J. H., Steuber, G. D., and Yeh, F. C., "Heat Transfer in Rotating Serpentine Passage with Selected Model Orientations for Smooth or Skewed Trip Walls," *Journal of Turbomachinery*, Vol. 116, No. 4, 1994, pp. 738–744.

[66]Zhang, Y. M., Han, J. C., Parsons, J. A., and Lee, C. P., "Surface Heating Effect on Local Heat Transfer in a Rotating Two-Pass Square Channel with 60° Angled Rib Turbulators," *Journal of Turbomachinery*, Vol. 117, No. 2, 1995, pp. 272–280.

[67]Parsons, J. A., Han, J. C., and Zhang, Y. M., "Effects of Model Orientation and Wall Heating Condition on Local Heat Transfer in a Rotating Two-Pass Square Channel With 90° Rib Turbulators," *International Journal of Heat and Mass Transfer*, Vol. 38, No. 7, 1995, pp. 1151–1159.

[68]Dutta, S., and Han, J. C., "Local Heat Transfer in Rotating Smooth and Ribbed Two-Pass Square Channels with Three Channel Orientations," *Journal of Heat Transfer*, Vol. 118, 1996, pp. 578–584.

[69]Park, C. W., Lau, S. C., and Kukreja, R. T., "Effect of Rib Size on Heat (Mass) Transfer Distribution in a Rotating Channel," American Society of Mechanical Engineers, 42nd International Gas Turbine and Aeroengine Congress and Exhibition, Orlando, FL, ASME Paper 97-AA-126, June 1997, pp. 1–7.

[70]Park, C. W., Lau, S. C., and Kukreja, R. T., "Heat (Mass) Transfer in a Rotating Channel with Ribs of Various Sizes on Two Walls," *Journal of Thermophysics and Heat Transfer*, Vol. 12, 1998, pp. 452–455.

[71]Taslim, M. E., Rahman, A., and Spring, S. D., "An Experimental Investigation of Heat Transfer Coefficients in a Spanwise Rotating Channel with Opposing Rib-Roughened Walls," *Journal of Turbomachinery*, Vol. 113, No. 1, 1991, pp. 75–82.

[72]Taslim, M. E., Bondi, L. A., and Kercher, D. M., "An Experimental Investigation of Heat Transfer in an Orthogonally Rotating Channel Roughened with 45° Criss-Cross Ribs on Two Opposite Walls," *Journal of Turbomachinery*, Vol. 113, No. 3, 1991, pp. 346–353.

[73]Azad, G. S., Uddin, M. J., Han, J. C., Moon, H.-K., and Glezer, B., "Heat Transfer in a Two-Pass Rectangular Rotating Channel with 45° Angled Rib Turbulators," American Society of Mechanical Engineers, 46th International Gas Turbine and Aeroengine Congress and Exhibition, New Orleans, LA, ASME Paper 2001-GT-186, June 2001, pp. 1–10.

[74]Griffith, T. A., Al-Hadhrami, L., and Han, J.-C., "Heat Transfer in Rotating Rectangular Cooling Channels (AR = 4) with Angled Ribs," *Journal of Heat Transfer*, Vol. 124, No. 3, 2002, pp. 756–855.

[75]Dutta, S., Han, J. C., and Lee, C. P., "Local Heat Transfer in a Rotating Two-Pass Ribbed Triangular Duct with Two Model Orientations," *International Journal of Heat and Mass Transfer*, Vol. 39, No. 4, 1996, pp. 707–715.

[76]Liou, T.-M., Chen, M.-Y., and Wang, Y.-M., "Heat Transfer, Fluid Flow, and Pressure Measurements Inside a Rotating Two-Pass Duct with Detached 90° Ribs," American Society of Mechanical Engineers, 47th International Gas Turbine and Aeroengine Congress and Exhibition, Amsterdam, ASME Paper GT-2002-30201, 2002, pp. 1–13.

[77]Bunker, R. S., Wetzel, T. G., and Rigby, D. L., "Heat Transfer in a Complex Trailing Edge Passage for a High Pressure Turbine Blade—Part 1: Experimental Measurements," American Society of Mechanical Engineers, 47th International Gas Turbine and Aeroengine Congress and Exhibition, Amsterdam, ASME Paper GT-2002-30212, June 2002, pp. 1–7.

[78]Bonhoff, B., Parneix, S., Leusch, J., Johnson, B. V., Schabacker, J., and Bolcs, A., "Experimental and Numerical Study of Developed Flow and Heat Transfer in Coolant Channels with 45 Ribs," *International Journal of Heat and Fluid Flow*, Vol. 20, 1999, pp. 311–319.

[79]Schabacker, J., Bolcs, A., and Johnson, B. V., "PIV Investigation of the Flow Characteristics in an Internal Coolant Passage with 45° Rib Arrangement," American Society of Mechanical Engineers, 44th International Gas Turbine and Aeroengine Congress and Exhibition, Indianapolis, IN, ASME Paper 99-GT-120, June 1999, pp. 1–8.

[80]Tse, D. G. N., and Steubner, G. D., "Flow in a Rotating Square Serpentine Coolant Passage with Skewed Trips," American Society of Mechanical Engineers, 42nd International Gas Turbine and Aeroengine Congress and Exhibition, Orlando, FL, ASME Paper 97-GT-529, June 1997, pp. 1–8.

[81]Prabhu, S. V., and Vedula, R. P., "Pressure Drop Distribution in a Rotating Rectangular Channel with One Ribbed Surface," American Society of Mechanical Engineers, 42nd International Gas Turbine and Aeroengine Congress and Exhibition, Orlando, FL, ASME Paper 97-GT-118, June 1997, pp. 1–9.

[82]Prakash, C., and Zerkle, R., "Prediction of Turbulent Flow and Heat Transfer in a Ribbed Rectangular Duct with and Without Rotation," *Journal of Turbomachinery*, Vol. 117, No. 2, 1995, pp. 255–264.

[83]Stephens, M. A., Chyu, M. K., and Shih, T. I.-P., "Computations of Convective Heat Transfer in a Square Duct with Inclined Ribs of Rounded Cross Section," American Society of Mechanical Engineers, International Mechanical Engineering Congress and Exhibition, ASME Paper 96-WA/HT-12, Nov. 1996, pp. 1–8.

[84]Rigby, D. L., Steinthorsson, E., and Ameri, A. A., "Numerical Prediction of Heat Transfer in a Channel with Ribs and Bleed," American Society of Mechanical Engineers, 42nd International Gas Turbine and Aeroengine Congress and Exhibition, Orlando, FL, ASME Paper 97-GT-431, June 1997, pp. 1–8.

[85]Iacovides, H., "Computation of Flow and Heat Transfer Through Rotating Ribbed Passage," *International Journal of Heat and Fluid Flow*, Vol. 19, 1998, pp. 393–400.

[86]Jia, R., Saidi, A., and Sunden, B., "Heat Transfer Enhancement in Square Ducts with V-Shaped Ribs of Various Angles," American Society of Mechanical Engineers, 47th International Gas Turbine and Aeroengine Congress and Exhibition, Amsterdam, ASME Paper GT-2002-30209, June 2002, pp. 1–8.

[87]Watanabe, K., and Takahashi, T., "LES Simulation and Experimental Measurement of Fully Developed Ribbed Channel Flow and Heat Transfer," American Society of Mechanical Engineers, 47th International Gas Turbine and Aeroengine Congress and Exhibition, Amsterdam, ASME Paper GT-2002-30203, June 2002, pp. 1–8.

[88]Al-Qahtani, M., Chen, H.-C., and Han, J. C., "A Numerical Study of Flow and Heat Transfer in Rotating Rectangular Channels (AR = 4) with 45° Rib Turbulators by Reynolds Stress Turbulence Model," American Society of Mechanical Engineers, 47th International Gas Turbine and Aeroengine Congress and Exhibition, Amsterdam, ASME Paper GT-2002-30216, June 2002, pp. 1–10.

[89]Al-Qahtani, M., Jang, Y., Chen, H. C., and Han, J. C., "Prediction of Flow and Heat Transfer in Rotating Two-Pass Rectangular Channels with 45° Rib Turbulators," American Society of Mechanical Engineers, 46th International Gas Turbine and Aeroengine Congress and Exhibition, New Orleans, LA, ASME Paper 2001-GT-187, June 2001, pp. 1–11.

[90]Bonhoff, B., Tomm, U., Johnson, B. V., and Jennions, I., "Heat Transfer Predictions for Rotating U-Shaped Coolant Channels with Skewed Ribs and with Smooth Walls," American Society of Mechanical Engineers, 42nd International Gas Turbine and Aeroengine Congress and Exhibition, Orlando, FL, ASME Paper 97-GT-162, June 1997, pp. 1–8.

[91]Stephens, M. A., and Shih, T. I.-P., "Computation of Compressible Flow and Heat Transfer in a Rotating Duct with Inclined Ribs and 180 Degree Bend," American Society of Mechanical Engineers, 42nd International Gas Turbine and Aeroengine Congress and Exhibition, Orlando, FL, ASME Paper 97-GT-192, June 1997, pp. 1–9.

[92]Shih, T. I.-P., Lin, Y.-L., Stephens, M. A., and Chyu, M. K., "Flow and Heat Transfer in a Ribbed U-Duct Under Typical Engine Conditions," American Society of Mechanical Engineers, 43rd International Gas Turbine and Aeroengine Congress and Exhibition, Stockholm, ASME Paper 98-GT-213, June 1998, pp. 1–10.

[93]Rigby, D. L., "Prediction of Heat and Mass Transfer in a Rotating Ribbed Coolant Passage with a 180 Degree Turn," American Society of Mechanical Engineers, 43rd International Gas Turbine and Aeroengine Congress and Exhibition, Stockholm, ASME Paper 98-GT-329, June 1998, pp. 1–11.

[94]Lin, Y.-L., Shih, T. I.-P., Stephens, M. A., and Chyu, M. K., "A Numerical Study of Flow and Heat Transfer in a Smooth and a Ribbed U-Duct with and Without Rotation," *Journal of Heat Transfer*, Vol. 123, No. 2, 2001, pp. 219–232.

[95]Rigby, D. L., and Bunker, R. S., "Heat Transfer in a Complex Trailing Edge Passage for a High Pressure Turbine Blade—Part 2: Simulation Results," American Society of Mechanical Engineers, ASME Paper GT-2002-30213, 2002.

[96]Taslim, M. E., and Wadsworth, C. M., "An Experimental Investigation of the Rib Surface-Averaged Heat Transfer Coefficient in a Rib-Roughened Square Passage," *Journal of Turbomachinery*, Vol. 119, No. 2, 1997, pp. 381–389.

[97]Taslim, M. E., and Lengkong, A., "45 Deg Staggered Rib Heat Transfer Coefficient Measurements in a Square Channel," *Journal of Turbomachinery*, Vol. 120, No. 3, 1998, pp. 571–580.

[98]Ogawa, A., *Vortex Flow*, CRC Press, New York, 1993.

[99]Glezer, B., Moon, H.-K., and O'Connell, T., "A Novel Technique for the Internal Blade Cooling," American Society of Mechanical Engineers, ASME Paper 96-GT-181, 1996.

[100]Glezer, B., Moon, H.-K., Kerrebrock, J., Bons, J., and Guenette, G., "Heat Transfer in a Rotating Radial Channel with Swirling Internal Flow," American Society of Mechanical Engineers, ASME Paper 98-GT-214, 1998.

[101]Kreith, F., and Margolis, D., "Heat Transfer and Friction in Turbulent Vortex Flow," *Applied Scientific Research*, Vol. 8, Sec. A, 1959, pp. 457–473.

[102]Khalatov, A. A., and Zagumennov, I. M., "Heat Transfer and Fluid Dynamics Near Flat Surfaces in Confined Swirling Flows," *Proceedings of the Ninth International Heat Transfer Conference*, Jerusalem, Vol. 4, 1990, pp. 329–334.

[103]Ligrani, P. M., Hedlund, C. R., Thambu, R., Babinchak, B. T., Moon, H.-K., and Glezer, B., "Flow Phenomena in Swirl Chambers," *Experiments in Fluids*, Vol. 24, No. 3, 1998, pp. 254–264.

[104]Moon, H.-K., O'Connell, T., and Glezer, B., "Heat Transfer Enhancement in a Circular Channel Using Lengthwise Continuous Tangential Injection," *Proceedings of the Eleventh International Heat Transfer Congress*, Kyongju, Republic of Korea, Vol. 6, 1998, pp. 559–564.

[105]Date, A. W., "Prediction of Fully Developed Flow in a Tube Containing a Twisted-Tape," *International Journal of Heat and Mass Transfer*, Vol. 17, 1974, pp. 845–859.

[106]Hong, S. W., and Bergles, A. E., "Augmentation of Laminar Flow Heat Transfer in Tubes by Means of Twisted-Tape Inserts," *Journal of Heat Transfer*, Vol. 98, No. 2, 1976, pp. 251–256.

[107]Kumar, R., and Conover, T., "Flow Visualization Studies of a Swirling Flow in a Cylinder," *Experimental Thermal and Fluid Science*, Vol. 7, 1993, pp. 254–262.

[108]Dong, M., and Lilley, D. G., "Parameter Effects on Flow Patterns in Confined Turbulent Swirling Flows," *Computer Modeling, Cofiring and NOx Control*, FACT-Vol. 17, American Society of Mechanical Engineers, Fairfield, NJ, 1993, pp. 17–21.

[109]Bruun, H. H., Fitouri, A., and Khan, M. K., "The Use of a Multiposition Single Yawed Hot-Wire Probe for Measurements in Swirling Flow," *Thermal Anemometry*, FED-Vol. 167, American Society of Mechanical Engineers, Fairfield, NJ, 1993, pp. 57–65.

[110]Fitouri, A., Khan, M. K., and Bruun, H. H., "A Multiposition Hot-Wire Technique for the Study of Swirling Flows in Vortex Chambers," *Experimental Thermal and Fluid Science*, Vol. 10, 1995, pp. 142–151.

[111]Chang, F., and Dhir, V. K., "Turbulent Flow Field in Tangentially Injected Swirl Flows in Tubes," *International Journal of Heat and Fluid Flow*, Vol. 15, No. 5, 1994, pp. 346–356.

[112]Sampers, W. F. J., Lamers, A. P. G. G., and Van Steenhoven, A. A., "Experimental and Numerical Analysis of a Turbulent Swirling Flow in a Tube," *ICHEME Symposium Series No. 129*, Vol. 2, 1992, pp. 765–771.

[113]Li, H., and Tomita, Y., "Characteristics of Swirling Flow in a Circular Pipe," *Journal of Fluids Engineering*, Vol. 116, No. 2, 1994, pp. 370–373.

[114]Kok, J. B. W., Rosendal, F. J. J., and Brouwers, J. J. H., "LDA—Measurements on Swirling Flows in Tubes," *SPIE Laser Anemometry Advances and Applications*, Vol. 2052, 1993, pp. 721–728.

[115]Gambill, W. R., and Bundy, R. D., "An Evaluation of the Present Status of Swirl-Flow Heat Transfer," American Society of Mechanical Engineers, ASME–AIChE Heat Transfer Conf. and Exhibit, Houston, TX, ASME Paper 62-HT-42, Aug. 1962, pp. 1–12.

[116]Bergles, A. E., "Survey and Evaluation of Techniques to Augment Convective Heat and Mass Transfer," *International Journal of Heat and Mass Transfer*, Vol. 1, 1969, pp. 331–413.

[117]Razgaitis, R., and Holman, J. P., "A Survey of Heat Transfer in Confined Swirling Flows," *Future Energy Production Systems, Heat and Mass Transfer Processes*, Vol. 2, Academic Press, New York, 1976, pp. 831–866.

[118]Papadopoulos, P., France, D. M., and Minkowycz, W. J., "Heat Transfer to Dispersed Swirl Flow of High-Pressure Water with Low Wall Super Heat," *Experimental Heat Transfer*, Vol. 4, No. 1, 1991, pp. 153–169.

[119]Hedlund, C. R., Ligrani, P. M., Moon, H.-K., and Glezer, B., "Heat Transfer and Flow Phenomena in a Swirl Chamber Simulating Turbine Airfoil Internal Cooling," *Journal of Turbomachinery*, Vol. 121, No. 4, 1999, pp. 804–813.

[120]Hedlund, C. R., and Ligrani, P. M., "Local Swirl Chamber Heat Transfer and Flow Structure at Different Reynolds Numbers," *Journal of Turbomachinery*, Vol. 122, No. 2, 2000, pp. 375–385.

[121]Khalatov, A., Syred, N., Bowen, P., Al-Ajmi, R., Kozlov, A., and Schukin, A., "Innovative Cyclone Cooling Scheme for Gas Turbine Blade: Thermal-Hydraulic Performance Evaluation," American Society of Mechanical Engineers, International Gas Turbine and Aeroengine Congress and Exhibition, Munich, ASME Paper 2000-GT-237, May 2000, pp. 1–11.

[122]Hwang, J.-J., and Cheng, C.-S., "Augmented Heat Transfer in a Triangular Duct by Using Multiple Swirling Jets," *Journal of Heat Transfer*, Vol. 121, No. 3, 1999, pp. 683–690.

[123]Belnap, B. J., van Rij, J. A., and Ligrani, P. M., "A Reynolds Analogy for Real Component Surface Roughness," *International Journal of Heat and Mass Transfer*, Vol. 45, No. 15, 2002, pp. 3089–3099.

[124]van Rij, J. A., Belnap, B. J., and Ligrani, P. M., "Analysis and Experiments on Three-Dimensional, Irregular Surface Roughness," *Journal of Fluids Engineering*, Vol. 124, No. 3, 2002, pp. 671–677.

[125]Gee, D. L., and Webb, R. L., "Forced Convection Heat Transfer in Helically Rib-Roughened Tubes," *International Journal of Heat and Mass Transfer*, Vol. 23, 1980, pp. 1127–1136.

G. M. Faeth
Past Editor-in-Chief